

1
2
3
4
5
6
7
8
9
10
11
12
13
14
15
16
17
18
19
20
21
22
23
24
25
26
27
28
29
30

A drug repurposing screen identifies altiratinib as a selective inhibitor of a key regulatory splicing kinase and a potential therapeutic for toxoplasmosis and malaria

Christopher Swale^{1†*}, Valeria Bellini^{1†}, Matthew W. Bowler², Nardella Flore³, Marie-Pierre Brenier-Pinchart¹, Dominique Cannella¹, Lucid Belmudes⁴, Caroline Mas⁵, Yohann Couté⁴, Fabrice Laurent⁶, Artur Scherf³, Alexandre Bougdour^{1*} and Mohamed-Ali Hakimi^{1*}

¹ Institute for Advanced Biosciences (IAB), Team Host-pathogen interactions and immunity to infection, INSERM U1209, CNRS UMR5309, University Grenoble Alpes, Grenoble, France

² European Molecular Biology Laboratory, Grenoble, 71 Avenue des Martyrs, CS 90181, 38042 Grenoble, France.

³ Institut Pasteur, Université de Paris, Unité de Biologie des Interactions Hôte-Parasite, CNRS ERL 9195, INSERM U1201, F-75015 Paris, France.

⁴ Univ. Grenoble Alpes, INSERM, CEA, UMR BioSanté U1292, CNRS, CEA, FR2048 38000, Grenoble, France.

⁵ Integrated Structural Biology Grenoble (ISBG) CNRS, CEA, Université Grenoble Alpes, EMBL, 71 avenue des Martyrs, F-38042, Grenoble, France.

⁶ INRAE, Université François Rabelais de Tours, Centre Val de Loire, UMR1282 ISP, Laboratoire Apicomplexes et Immunité Mucosale, 37380 Nouzilly, France.

[†]These authors contributed equally to this work.

* Correspondence to:

mohamed-ali.hakimi@univ-grenoble-alpes.fr - ORCID: 0000-0002-2547-8233

alexandre.bougdour@univ-grenoble-alpes.fr - ORCID: 0000-0002-5895-0020

christopher.swale@univ-grenoble-alpes.fr - ORCID: 0000-0002-9739-7774

Key words: *Toxoplasma gondii*, *Plasmodium falciparum*, drug repurposing, kinase, splicing

31 **Introductory paragraph**

32 The apicomplexa comprise a large phylum of single-celled, obligate intracellular protozoa that
33 infect humans and animals and cause severe parasitic diseases. Available therapeutics against
34 these devastating diseases are limited by suboptimal efficacy and frequent side effects, as well
35 as the emergence and spread of resistance. Here, we use a drug repurposing strategy and identify
36 altiratinib, a compound originally developed to treat glioblastoma, as a promising drug
37 candidate with broad spectrum activity against apicomplexans. Altiratinib is parasitocidal and
38 blocks the development of intracellular zoites in the nanomolar range and with a high selectivity
39 index. We have identified *TgPRP4K* of *T. gondii* as the primary target of altiratinib by genetic
40 target deconvolution, highlighting key residues within the kinase catalytic site that, when
41 mutated, confer resistance to the drug. We have further elucidated the molecular basis of the
42 inhibitory mechanism and species selectivity of altiratinib for *TgPRP4K* as well as for its *P.*
43 *falciparum* counterpart *PfCLK3*. Our data also point to structural features critical for binding
44 of the other *PfCLK3* inhibitor, TCMDC-135051. Consistent with the role of this kinase family
45 in splicing in a broad spectrum of eukaryotes, we have shown that altiratinib causes global
46 disruption of splicing, primarily through intron retention in both *T. gondii* and *P. falciparum*.
47 Thus, our data establish parasitic PRP4K/CLK3 as a promising pan-apicomplexan target whose
48 repertoire of inhibitors can be expanded by the addition of altiratinib.

50 **Introduction**

51 Infectious diseases caused by apicomplexan parasites remain the leading cause of morbidity
52 and mortality around the world, but with even more devastating consequences in low-income
53 countries, underscoring the need for effective medicines (De Rycker *et al.*, 2018). Indeed,
54 *Plasmodium falciparum* causes malaria in over 200 million people worldwide and is
55 responsible for more than 405 000 deaths in 2019 (WHO, World Malaria Report). Similarly,
56 *Toxoplasma gondii*, the causative agent of toxoplasmosis, causes widespread zoonotic
57 infection, with nearly one-third of the world's population being seropositive for this parasite.
58 In healthy adults, the acute infection resolves rapidly, leaving a chronic, subclinical infection.
59 However, in the absence of sustained immunity, reactivation of latent forms of *T. gondii* leads
60 to severe, life-threatening disease, as has been observed in AIDS, organ transplant or
61 chemotherapy patients, with a high mortality rate if no treatment is given (Montoya and
62 Liesenfeld, 2004). More severe cases may also occur following congenital transmission of the
63 parasite to the unborn child. In addition, *Toxoplasma gondii*, together with other coccidian

64 parasites, e.g. *Eimeria* spp. and *Neospora caninum*, are of veterinary importance as they cause
65 significant economic losses in livestock.

66

67 For many of these apicomplexa-mediated diseases, current treatments are suboptimal, and for
68 some there are few, if any, alternatives. Indeed, current standard treatment for toxoplasmosis is
69 hampered by severe side effects, particularly in immunocompromised individuals (Dunay *et*
70 *al.*, 2018). For malaria, artemisinin-based combination therapies (ACT) are currently used as
71 first-line treatments in endemic countries worldwide, but the emergence and spread of
72 resistance not only to artemisinin but also to the drug combinations is a growing threat (De
73 Rycker *et al.*, 2018). The frequent side effects and the ever-present threat of drug resistance
74 have led to the search for other therapeutic alternatives. Older drugs have recently made a
75 comeback by being repurposed for new diseases to accelerate drug development. After
76 phenotypic screening for drug repurposing, new indications for existing drugs can be quickly
77 identified and clinical trials can be rapidly conducted. Identifying the target and understanding
78 the mechanism of action is a critical bottleneck in drug development. Recent advances in
79 genomics and target deconvolution strategies have shifted the problem to a plethora of putative
80 targets awaiting clarification.

81

82 Here, we report the identification of altiratinib from a library of approved drugs that exhibits
83 potent, nanomolar, broad-spectrum anti-apicomplexan activity with a high selectivity index.
84 Altiratinib was in phase 1 clinical development for the treatment of invasive solid tumors,
85 including glioblastoma (Kwon Y *et al.* 2015; Smith DB *et al.* 2015). Using a genetic target-
86 deconvolution strategy, we identified *T. gondii* TgPRP4K, the closest relative of the human
87 splicing factor kinase PRP4 kinase (PRP4K/PRPF4B) and *Plasmodium falciparum* PfCLK3
88 (Alam MM *et al.* 2019; Mahindra A *et al.* 2020), as the primary target of altiratinib. Using an
89 integrated structural biology approach, we further elucidated the molecular basis for the
90 mechanism of inhibition of altiratinib and the remarkable selectivity for the parasitic
91 PRP4K/CLK3 enzymes. This kinase family plays a critical role in cell cycle progression by
92 regulating pre-mRNA splicing in all eukaryotic lineages (Schneider M *et al.* 2010; Lützelberger
93 M and Käufer NF, 2012; Corkery DP *et al.* 2015; Eckert D *et al.* 2016). Accordingly, altiratinib
94 causes global disruption of splicing with exon skipping, intron retention, and premature
95 transcription termination in both *T. gondii* and *P. falciparum*, but not in *Cryptosporidium*
96 *parvum*, in which the kinase has significantly divergent variations that may result in resistance

97 to altiratinib. Overall, our findings support this family of parasitic kinases as a promising
98 apicomplexan target and highlight the structural determinants that explain the remarkable
99 selectivity of altiratinib.

100

101 **Results**

102 **A drug repurposing screen identifies altiratinib as a potent and selective apicomplexan** 103 **inhibitor of parasite growth**

104 To identify new drug candidates against toxoplasmosis and potential targets, we screened a
105 small library of approved drugs for their ability to inhibit tachyzoite growth. All compounds
106 are structurally diverse, cell permeable, medically active, and commercially available
107 (Supplementary Table 1). Screening was performed in duplicate at 5 μ M while pyrimethamine
108 was used as a reference drug and blocked the growth of parasites as expected. The compounds
109 that showed reproducible inhibition of parasite growth of >70% were selected for further testing
110 (Extended Data Fig. 1a). Of the 432 compounds in the collection, 84 primary hits were found
111 to inhibit parasite growth without detectable cytotoxicity to the host cell (Fig. 1a), preferentially
112 targeting the cell cycle and tyrosine kinase/adaptor signaling pathways (Extended Data Fig. 1b;
113 Supplementary Table 1). A second screen at 1 μ M of the 84 compounds identified 14 molecules
114 with EC₅₀ in the nM range (Fig. 1b). The most potent growth inhibitor we identified was
115 altiratinib (DCC-2701, DP -5164, Fig. 1c) with an EC₅₀ of 28 nM against tachyzoites, which is
116 11-fold lower than pyrimethamine (300 nM), the standard treatment for toxoplasmosis (Fig.
117 1d). Altiratinib-treated parasites were smaller than the control group and no longer divided, as
118 no daughter cells were detectable (Fig. 1e). Plaque assays showed sustained inhibition of
119 parasite growth, as plaques could no longer be detected in the presence of altiratinib, suggesting
120 a defect in one or more steps of the lytic cycle (Extended Data Fig. 1d). Interestingly, we did
121 not observe regrowth after discontinuation of altiratinib, suggesting that the drug has a cidal
122 effect in contrast to pyrimethamine (Extended Data Fig. 1d). Remarkably, altiratinib showed
123 low host cytotoxicity, resulting in a high selectivity index (SI) with a value of 400 for human
124 primary fibroblasts (Fig. 1f; Extended Data Fig. 1c). Altiratinib is also effective in inhibiting
125 the growth of coccidial parasites of veterinary importance such as *Eimeria tenella* (Fig. 1g) and
126 *Neospora caninum* (Fig. 1h), as well as *P. falciparum*, although its efficacy is lower compared
127 with the antimalarial drug dihydroartemisinin (DHA) (Fig. 1i).

128

129 **Altiratinib target deconvolution by EMS-based mutagenesis-based forward genetic** 130 **screen**

131 Altiratinib was originally identified to inhibit tumor growth and invasion in a bevacizumab-
132 resistant glioblastoma mouse model and was in phase 1 clinical development for the treatment
133 of invasive solid tumors. The drug was predicted to be a pan-tyrosine kinase inhibitor of MET,
134 TIE2, VEGFR2, and TRK (Kwon Y et al. 2015; Smith DB et al. 2015), but none of these kinases
135 are conserved in apicomplexa. Therefore, to explore the mechanism of action of altiratinib in
136 *T. gondii*, we performed a forward genetic screen combining chemical mutagenesis and RNA
137 sequencing, as previously described (Bellini et al., 2020) (Extended Data Fig. 1e). Altiratinib-
138 resistant parasites were generated in 6 independent chemical mutagenesis experiments using 7
139 mM ethyl methanesulfonate (EMS) followed by selection in the presence of 300 nM altiratinib,
140 i.e. 10-fold the EC₅₀ value, for approximately 4 weeks. The resistant parasite lines were then
141 cloned by limited dilution and a single clone from each mutagenesis experiment (designated A
142 to F) was analyzed by whole-genome RNA sequencing (RNA-Seq). To map the EMS-induced
143 mutations conferring resistance to altiratinib, Illumina sequencing reads were aligned to the *T.*
144 *gondii* *GT1* reference genome. Using the parental strain as a reference, single nucleotide
145 variations (SNVs) were identified in the assembled sequences of the resistant mutants (see
146 *Materials and Methods*). By focusing on mutations in coding sequences, a single gene,
147 *TGGT1_313180*, contained SNVs that resulted in amino acid changes (F647S, L686F, L715F)
148 not present in the parental strain in five of the six drug-resistant lines (Fig. 2a,b and
149 Supplementary Table 2).

150
151 *TGGT1_313180* encodes a 928 amino acid (aa) protein that has a predicted kinase domain in
152 its C-terminus, hereafter referred to as *TgPRP4K* (Fig. 2b). *TgPRP4K* is phylogenetically
153 related to the cyclin-dependent-like kinase family (CLK) (Talevich, E. et al. 2011; Zhou Z and
154 Fu XD, 2013) and its closest ancestor in humans is the splicing factor kinase PRP4 kinase
155 (PRP4K or PRPF4B) and in *P. falciparum* is *PfCLK3* (*PF3D7_1114700*), a kinase that has
156 been identified as a multistage cross-species antimalarial drug target (Extended Data Fig. 2a)
157 (Agarwal, S. et al. 2011 ; Alam MM et al. 2019; Mahindra A et al. 2020). Immunofluorescence
158 analysis of intracellular parasites showed that *TgPRP4K* is localized to nuclear speckle-like
159 structures (Fig. 2c). *TgPRP4K* is essential for the lytic cycle of tachyzoites, as its genetic
160 deletion results in a fitness score of -4.69 (Sidik et al., 2016), and conditional deletion of the

161 kinase using the auxin-inducible degron system (AID) significantly impairs parasite growth
162 (Fig. 2d) in agreement with a recent study (Lee VV et al. bioRxiv preprint).

163

164 Surprisingly, the altiratinib-resistant parasite line from mutagenesis F has a wild-type (WT)
165 allele of *TgPRP4K* and a mutation E1325K in *TgPRP8*, a protein located in the catalytic core
166 of the spliceosome that has been shown to interact with PRP4K in *Schizosaccharomyces pombe*
167 to facilitate spliceosome activation (Bottner et al., 2005; Charenton C et al., 2019). This
168 reinforces the possibility that the PRP4K-PRP8 complex is at the basis for the anti-*Toxoplasma*
169 activity of altiratinib. The specific association between *TgPRP4K* and *TgPRP8* was then
170 confirmed by FLAG affinity immunoprecipitation and mass spectrometry (MS)-based
171 proteomic analyzes using knock-in parasite lines expressing a tagged version of each protein
172 (Supplementary Table 3). Other partners have been identified as pre-mRNA splicing proteins
173 constitutive of the core spliceosome, such as U2 snRNP proteins and U5 snRNP proteins,
174 including the RNA helicase Brr2 and Snu114, which forms a pocket enclosing the catalytic
175 RNA network of activated spliceosomes (Supplementary Fig. 1) (Bertram K et al., 2017;
176 Charenton C et al., 2019). Known pre-mRNA splicing factors were also purified along with
177 PRP4K and PRP8 (Supplementary Table 3 and Fig. 1). *TgPRP4K* was found in a high
178 molecular-weight complex (~500 kDa; fractions 24–26) that withstood stringent salt conditions
179 and partially co-eluted with the *TgPRP8*-containing spliceosome, which migrates by size
180 exclusion chromatography with an apparent molecular weight of ~900 kDa (fractions 18-20)
181 (Extended Data Fig. 2b, c).

182

183 **Mutations within *TgPRP4K* confer resistance to altiratinib**

184 To confirm that the mutations found in *TgPRP4K* and *TgPRP8* were sufficient to confer
185 resistance to altiratinib, we used the CRISPR/Cas9 system in conjunction with homology-
186 directed repair, to reconstruct each of the etiological mutations into the susceptible parental *T.*
187 *gondii* strain (Bellini et al., 2020). Parasites were cotransfected with a vector expressing the
188 Cas9 endonuclease and a synthetic guide RNA (sgRNA) targeting either *TgPRP4K* or *TgPRP8*,
189 and the corresponding homologous single-stranded donor oligonucleotides (ssODN) as repair
190 templates (Extended Data Fig. 3a). After altiratinib selection, the resistant parasites were
191 cloned, and DNA sequencing confirmed that the mutations were properly introduced at the
192 *TgPRP4K* locus (Extended Data Fig. 3b). Note that despite numerous attempts, allelic
193 substitution for *TgPRP8* could not be achieved, suggesting that the *TgPRP8* (E1325K) mutation

194 alone does not confer resistance to altiratinib and was not investigated further. Compared with
195 WT parasites, mutant strains edited for *TgPRP4K* (mutations F647S, L686F, and L715F)
196 significantly decreased sensitivity to altiratinib by 50- to 180-fold (Fig. 2e-g and Extended Data
197 Fig. 3c), suggesting that altiratinib targets *TgPRP4K* activity.

198

199 **Structural investigation of the mechanism of action of altiratinib on *TgPRP4K***

200 To unravel the molecular mechanism of action of altiratinib inhibition, we expressed the
201 predicted kinase domain of *TgPRP4K* in the WT and L715F variant versions by removing the
202 intrinsically disordered region at the N-terminus (Extended Data Fig. 4a). Both recombinant
203 proteins were produced in satisfactory yields, with the notable difference being a higher size
204 homogeneity of the L715F mutant (Extended Data Fig. 4b) when analyzed by size exclusion
205 chromatography coupled to laser light scattering (SEC-MALLS). The same sample did not
206 display a double band which can be seen in the WT (Extended Data Fig. 4c) and was also
207 observed in Flag-purified human WT PRPF4B as a result of posttranslational modifications
208 (Dellaire et al., 2002). The L715F mutation is peculiar because it centered on the DFG motif,
209 which is a DLG in apicomplexan parasites and plays a central role in regulating the activation
210 loop. Using a thermal stability assay and a thermophoresis titration assay, we could show a
211 direct stabilizing effect (delta Tm of 11 °C) and binding (Kd of 4 μM) of altiratinib with the WT
212 *TgPRP4K* kinase domain (Fig. 3a, b). Counterintuitively though, the L715F mutation does not
213 decrease altiratinib binding, but instead increases binding affinity (Fig. 3a, b). This not only
214 increases the apparent Kd value by almost a factor of 10, but also increases the stabilizing effect
215 of the compound *in vitro* compared to WT (with a delta Tm of 15 °C). This extraordinary
216 observation highlights an unusual resistance mechanism that compensates for the inhibitory
217 mechanism regardless of the binding affinity of the compound. Using this point mutant, we
218 successfully co-crystallized *TgPRP4K* in complex with altiratinib and obtained high-resolution
219 diffraction to 2.2 Å (pdb id: 7Q4A, Supplementary Table 4). A molecular replacement solution
220 was found with the human homolog of PRPF4B kinase domain (pdb id: 6CNH), which shares
221 47% sequence identity with *TgPRP4K*. The structure solution showed *TgPRP4K* crystallizing
222 as a dimer with the catalysis cavities facing each other (Extended Data Fig. 5a). The monomer
223 B exhibited more complete density within the flexible regions, so all further structural
224 representations are based on this monomer. The activation loop was fully assembled in our
225 model and occupies a DFG “out” conformation (Fig. 3c, Extended Data Fig. 5c) while the
226 tyrosine 729 is phosphorylated in this structure (Fig. 3c, Extended Data Fig. 5b). Interestingly,

227 this phospho-tyrosine is central to the ability of *Tg*PRP4K to crystallize under these conditions,
228 as it forms numerous crystal contacts with other symmetry-related molecules (**Extended Data**
229 **Fig. 5b**).

230
231 The activation loop displays an alpha helix (Ile 726 to Tyr 735) that appears to be unique to *T.*
232 *gondii* PRP4K when compared to the human ortholog, which was only ever crystallized in DFG
233 “in” conformations and is largely a random coil in this state (**Fig. 3c**, **Extended Data Fig. 5c**).
234 Compared to the human ortholog in its global structure, *Tg*PRP4K is structurally conserved,
235 with minor structural differences in the C-terminal portion (aa 840 to 854) of the kinase domain
236 (**Extended Data Fig. 5c**). The structure also reveals a C-terminal antiparallel short beta strand
237 that, to our knowledge, is unique to the PRP4K kinase lineage (**Fig. 3c**) and is also structurally
238 conserved in the human ortholog (**Extended Data Fig. 5c**), although sequence conservation is
239 very low.

240
241 Electron density for altiratinib was clearly visible in our crystal structure and interacts in the
242 ATP-binding pocket located at the interface between the N- and C-lobes (**Fig. 3c**), with the
243 DFG motif and the G-rich loop closing off this cavity. Remarkably, both monomers display
244 strong electron density for altiratinib, allowing us to confidently assign the entire molecule
245 (**Extended Data Fig. 6a**). More detailed analysis revealed that the interaction of the compound
246 within the cavity relies on numerous hydrophobic interactions (**Fig. 3d**, **Extended Data Fig. 6b**
247 **and 6c**), which can be divided into three distinct zones. The first zone, consisting of a
248 cyclopropanecarbonylamino group connecting a pyridine ring, interacts mainly with side chains
249 W649, L650, W651, L702 and A595 (**Fig. 3d**, **Extended Data Fig. 6c**). Hydrogen bonds also
250 form with the carbonyl and amide groups of the leucine 650, and most of these residues form
251 the ATP-binding hinge region leading to the deeper allosteric pocket. The second zone of
252 altiratinib is central and consists mainly of a difluorophenyl ring stacked between the two
253 phenylalanines 647 and 715 (the DFG central residue, which is a leucine in wild type *Tg*PRP4K)
254 (**Fig. 3d**), with one of the fluorine groups interacting with the sulfur group of C713 (**Extended**
255 **Data Fig. 6c**). These interactions ensure that the activation loop remains in this « out » position.
256 Finally, the last part of altiratinib which encompasses a cyclopropane-1,1-dicarboxamide
257 leading to a fluorophenyl ring, is buried deep in the allosteric cavity and interacts with multiple
258 residues within the C-lobe, notably the glutamic acid 612 and leucine 616 and 619, which line
259 up on the C-alpha-helix (**Fig. 3d**, **Extended Data Fig. 6c**). Other interactions are mediated by

260 I630 and L686, as well as the H693, which belongs to the canonical Hx/D triad that is a H/A/D
261 in PRP4K proteins. Only one residue within the N-lobe, the catalytic lysine K597, forms a
262 hydrogen bond with the central carboxy group. Using this structure, we can now rationalize the
263 consequences of the resistance mutations triggered by our EMS screen. All of the point
264 mutations we obtained involve residues that interact directly with altiratinib, whereas the direct
265 mechanisms of resistance are likely quite different (Fig. 3e). The L686F mutation logically
266 introduces a steric hindrance for the fluorophenyl ring by significantly increasing the size of
267 the side-chain. The other two resistance-conferring mutations, F647S and L715F, involve
268 residues in direct interaction and at opposite sides of the central difluorophenyl ring. F647S
269 probably strongly decreases hydrophobic stacking, while we have evidence that the mutation
270 L715F does not cause steric hindrance but, on the contrary, probably increases hydrophobic
271 stacking of the difluorophenyl ring. However, within these mutants there is little evidence
272 pointing towards a species specificity, although altiratinib is not recognized as an inhibitor of
273 PRPF4B in human cells, as it was originally designed to inhibit the kinases MET, TIE2 (TEK),
274 and VEGFR2 (KDR) (Kwon Y et al. 2015; Smith DB et al. 2015). Of the residues involved in
275 binding to altiratinib, most are strictly conserved among PRPF4B orthologs (Fig. 3e), but the
276 hinge region has residues (W649 and W651) that diverge considerably from the human
277 ortholog, being replaced by a proline and serine, respectively.

278

279 **Hinge region residue 649 controls species specificity of altiratinib towards TgPRP4K**

280 The superposition of the human and *T. gondii* PRPF4B/PRP4K structures makes it clear that
281 the hinge region has a consistent backbone structure despite significant differences in side chain
282 composition (Fig. 4a). More importantly, this overlay shows that the change from W649 to
283 P769 would affect the main hydrophobic component that stacks the
284 cyclopropanecarbonylamino and pyridin groups of altiratinib. A similar, albeit lesser, role can
285 also be attributed to W651, whose equivalent residue in humans is S771 and likely reduces the
286 hydrophobic caging potential toward altiratinib. To test the significance of residue W649, we
287 used the same CRISPR-Cas9 complementation approach for SNP validation to generate a
288 “humanised” mutant W649/P that requires a codon change from TGG to CCG (Fig. 4b). The
289 probability of such a change occurring in EMS mutagenesis is low because a change from G to
290 C is required between two replaced nucleotides. This substitution is not prevalent in EMS
291 mutagenesis, which preferentially alkylates G residues (Greene EA et al. 2003). Remarkably,
292 this artificial humanization produced parasites that were resistant to altiratinib (Fig. 4c-e) and
293 had an EC₅₀ of 3.5 μM, which is comparable to the mutations using the EMS approach. Finally,

294 using *TgPRP4K* WT, L715F and W649P expressed in insect cells, we were able to probe the *in*
295 *vitro* consequences of these two different mutations on the ability of the protein to interact with
296 altiratinib. Using an indirect thermal shift assay (Fig. 4f, h) and a thermophoresis approach (Fig.
297 4g), we demonstrated that the hydrophobic stacking of W649 is essential for altiratinib binding,
298 as almost no stabilization is observed in the presence of altiratinib (delta Tm of 3 °C), compared
299 to WT PRPF4B (Delta Tm of 11°C), while the binding affinity measured in thermophoresis
300 transitions from 4 μM to not measurable.

301

302 **Chemical inactivation of *TgPRP4K* activity disturbs pre-mRNA splicing in *T. gondii***

303 Since it has been proposed that the human kinase PRPF4B and *PfCLK3* regulate RNA splicing
304 (Schneider M *et al.* 2010; Alam *et al.* 2019), we examined transcriptional changes in the
305 parental parasite RH and in the drug-resistant strains L715F and W649P in response to exposure
306 to altiratinib using nanopore long-read direct RNA sequencing (DRS), a technology well suited
307 for determining the full repertoire of mRNA species, including alternative splicing isoforms
308 and divergent patterns, if present. The most obvious effect was that a substantial number of
309 genes (n=2400) showed altered mRNA expression, of which 784 were induced and 1616
310 suppressed when the parent strain was treated with altiratinib, whereas no change was observed
311 in the two mutant strains exposed to the drug (Fig. 5a). This confirms that altiratinib disrupts
312 mRNA transcription, which was expected, but also that the drug specifically targets *TgPRP4K*,
313 as both mutations not only confer resistance (Fig. 2d-f) but also restore gene expression to the
314 untreated state (Fig. 5a). Having identified isoforms with high confidence using the Nanopore
315 data, we used FLAIR (Full-Length Alternative Isoform Analysis of RNA) (Tang AD *et al.*,
316 2020) as a framework for analyzing differential isoform usage in wild-type and mutant strains
317 left untreated or exposed to altiratinib. The most important transcriptional phenotype was the
318 change in pre-mRNA splicing dynamics associated with inhibition of *TgPRP4K* exclusively in
319 WT parasites (Fig. 5b). At many *loci*, chemical inactivation of *TgPRP4K* was accompanied by
320 complete retention of the second intron (e.g., *TGME49_214940*; Fig. 5b,d) or intron retention
321 and exon skipping at the same *loci* (e.g., *TGME49_211420* and *TGME49_247350*; Fig. 5c;
322 Extended Data Fig. 7a). When an intron is spliced, it rapidly promotes splicing of subsequent
323 introns, whereas when splicing is hindered, subsequent introns tend to be retained, leading to
324 the concept of ‘all or none’ splicing (Oesterreich FC *et al.* 2016; Herzel L *et al.* 2018).
325 Consistent with this concept, we regularly observed a global collapse of splicing along the entire
326 transcript (e.g., *TGME49_208450*; Extended Data Fig. 7b) after drug treatment.

327

328 Since splicing is predominantly cotranscriptional, we also observed that intron retention leads
329 to premature transcriptional termination (e.g., *TGME49_278940*; **Extended Data Fig. 7c**). At
330 the transcriptome level, intron retention is the predominant aberrant splicing event found in
331 altiratinib-treated WT tachyzoites in contrast to the host cells they infect, underscoring the high
332 degree of selectivity of altiratinib (**Fig. 5e**). Upon closer inspection, we found that intron
333 retention leads to premature termination of translation due to frameshifts, which may ultimately
334 lead to altered function of the protein-coding gene. In addition, aberrant isoforms are degraded,
335 as indicated by the lower read rates at some *loci*, likely through nonsense-mediated decay
336 (NMD), a quality control mechanism that eliminates transcripts with a premature termination
337 codon. In this way, treatment with altiratinib leads to the production of defective proteins that
338 ultimately affect parasite survival.

339

340 **Altiratinib also causes mis-splicing in *P. falciparum* but not in *C. parvum*, which has a** 341 **divergent PRP4K ortholog**

342 Because altiratinib was active against a wide range of apicomplexans (**Fig. 1**) and the
343 PRPK4/CLK3 family was well conserved within the phylum, we wondered whether the drug
344 might inhibit splicing in other parasites of the phylum. We first examined transcriptional
345 changes of red blood cells infected with *P. falciparum* after treatment with altiratinib using
346 Nanopore DRS. All types of splicing defects that we had observed in *T. gondii* were also present
347 in *P. falciparum*, such as exon skipping, intron retention, and premature transcription
348 termination (**Fig. 6a**; **Extended Data Fig. 8a-c**), with a general trend toward global splicing
349 collapse along the entire transcript, with premature mRNAs being highly susceptible to NMD
350 degradation (**Extended Data Fig. 8a-c**). As with *T. gondii*, markedly increased intron retention
351 is a conserved phenomenon in *P. falciparum* exposed to altiratinib (**Fig. 6b**). These results
352 underscore the potential targeting by altiratinib of *Pf*CLK3 (*PF3D7_1114700*), a kinase that is
353 essential for *P. falciparum* survival in red blood cells and plays a critical role in regulating RNA
354 splicing of the malaria parasite (Alam MM, 2019; Mahindra *et al.*, 2020). We then took the
355 opportunity to test the drug on *Cryptosporidium parvum*, a parasite of the phylum that differs
356 from others in having a significantly divergent ortholog of PRP4K/CLK3 (*cgd8_5180*),
357 specifically the resistance-conferring DFG motif instead of the DLG motif found in *T. gondii*
358 and *P. falciparum*, but also several significant mutations at other altiratinib-interacting residues
359 (L719 to F, W651 to H, and C713 to S) that may strongly affect the binding selectivity of
360 altiratinib (**Extended Data Fig. 2a** and **Extended Data Fig. 8d**). As expected, we observed no

361 defects in mRNA splicing in *C. parvum* exposed to altiratinib (Fig. 6c-d; Extended Data Fig.
362 8e), again confirming the selectivity of the drug for PRP4K/CLK3 with a DLG motif and ruling
363 out off-target activities.

364

365 **The ins and outs of CLK3/PRP4K inhibition by altiratinib or TCMDC-135051**

366 To further confirm *P. falciparum* PfCLK3/PRP4K as a target of altiratinib, we expressed the
367 WT PfPRP4K kinase domain to probe this biochemical interaction (Extended Data Fig. 9).
368 Using the previously described thermal shift assay, we found that altiratinib indeed stabilizes
369 PfCLK3, albeit with a weaker potential, the delta Tm is of 4°C, compared to TgPRP4K, which
370 has a delta Tm of 11°C (Fig. 6e). Interestingly, however, when probing the TCMDC-135051
371 compound, a recently discovered inhibitor of PfCLK3 (Mahindra *et al.*, 2021), we observed a
372 reversed trend with a stronger stabilizing effect on PfCLK3 with a delta Tm of 10°C instead of
373 7°C for TgPRP4K (Fig. 6e). These results highlight two important aspects. First, we confirm
374 that TCMDC-135051 likely binds the active site of PfCLK3 as the energy requirements for
375 such a stabilizing effect would probably only occur within a buried cavity strongly interacting
376 with the compound. Second, this also highlights that there may still be some species selectivity
377 between the two compounds. As we were unable to crystallize PfCLK3 in the bound or unbound
378 state, we used alphafold2 (Jumper *et al.*, 2021) within collabfold (Mirdita *et al.*, 2021) to
379 create a model that we superposed to our crystallographic structure and manually docked
380 TCMDC-135051, taking advantage of the structural homology to other hinge regions binders
381 containing a 7-azaindole scaffold (as initially proposed in Mahindra *et al.*, 2021). In this
382 modeling (Fig. 6f), we observe that most of the PRP4K/CLK3 hinge region is conserved
383 between *P. falciparum* and *T. gondii*, in particular residues W649/W647 in TgPRP4K, which
384 are also fully conserved in PfCLK3 (W446/W448) and likely also have an important impact on
385 the selectivity of TCMDC-135051, particularly through hydrophobic stacking. However, the
386 conformation of the activation loop is not consistent with the binding of TCMDC-135051 in
387 the TgPRP4K structure (Fig. 6f), indicating potential differences in the activation loop
388 conformation that may differ between TCMDC-135051 and altiratinib.

389

390 **Discussion**

391 Our studies define altiratinib as a promising pan-apicomplexan drug candidate effective against
392 the human pathogens *T. gondii* and *P. falciparum*, as well as *N. caninum* and *E. tenella* of
393 veterinary interest. Using genetic, structural and transcriptional approaches, we have shown

394 that repurposing of altiratinib disrupts mRNA splicing in *T. gondii* and *P. falciparum* by
395 targeting the kinase core of PRP4K/CLK3. The induced splicing defects are so extensive that
396 they lead to irreversible inhibition in the nanomolar range of rapidly proliferating apicomplexan
397 zoites in cellular assays. Using a genetic target-deconvolution strategy, we have highlighted
398 key residues involved in binding to altiratinib. Unexpectedly, this has allowed us to crystallize
399 and resolve the first structure of a previously elusive apicomplexan kinase PRP4K/CLK3. This
400 co-crystal structure allows us to assign an electron density to altiratinib located at the interface
401 between the N and C lobes and occupying both the ATP-binding site and the allosteric pocket,
402 a singular type of binding that holds PRP4K in a DFG-out conformation consistent with
403 inhibition of the type II kinases. The structural data have clarified many unanswered questions
404 related to the species selectivity of altiratinib, as we now know that its ability to discriminate
405 the human ortholog and bind the parasitic PRP4K/CLK3 is constrained by residues
406 W649/W651 in the hinge region (Fig. 4a), which have diverged significantly and are also likely
407 critical for binding of the recently discovered *Pf*CLK3 inhibitor TCMDC-135051 (Fig. 6f)
408 (Alam MM, 2019; Mahindra *et al.*, 2020). Another important divergence is the shift from DFG
409 to DLG that has occurred between mammals and some apicomplexans. DLG is indeed
410 associated with inactive or weakly active kinases such as ROR2 (Artim SC *et al.* 2012;
411 Mendrola JM, 2013), and the selective pressure that led to this mutation is not yet clear, as
412 DFG-mutated tachyzoites behave normally in cell cultures (Fig. 2d-f). This likely gain in
413 activity is sufficient to resist altiratinib, although binding affinities are increased.

414
415 Some open questions remain to be answered. Although the evidence for a direct interaction
416 between altiratinib and PRP4K/CLK3 and drug-induced mis-splicing is overwhelming, the true
417 mechanism of spliceosome inhibition is still in question, as PRP4K not only plays a role in pre-
418 B spliceosome activation by phosphorylating other components of PRP, notably PRP6 and
419 PRP31 (Schneider *et al.* 2010), but also structurally integrates the complex (Charenton C *et al.*,
420 2019) and contacts the RNase PRP8, which may be allosterically involved in its activity.
421 Inhibition of activity or conformational entrapment (or both) may therefore be the key to proper
422 inhibition. *Pf*CLK3 has been identified as a multistage cross-species malarial drug target and
423 TCMDC-135051 a drug candidate with a high curative and transmission-blocking potential
424 (Alam MM, 2019; Mahindra *et al.*, 2020). Altiratinib and TCMDC-135051 have a very
425 different chemical space and although they rely on comparable elements within the hinge region
426 to selectively bind apicomplexan PRP4K/CLK3, species selectivity is still present, possibly due

427 to differences in the dynamics of the activation loop with which binding is compatible. Dual
428 (SAR)-directed optimization will therefore open the possibility of developing a pan-
429 apicomplexan therapy based on the altiratinib/TCMDC-135051 combination.

430

431 Our work highlights the utility of drug repurposing and provides structural mechanistic insights
432 into understanding how the PRP4K/CLK3 family is susceptible to selective pharmacological
433 inhibition by small drug-like molecules. This opens new opportunities to chemically improve
434 existing molecules to optimize pathogen killing via the PRP4K/CLK3 pathway.

435

436 **Methods**

437 ***Toxoplasma gondii*, *Plasmodium falciparum* and human cell culture.** Human primary
438 fibroblasts (HFFs, ATCC® CCL-171™) were cultured in Dulbecco's Modified Eagle Medium
439 (DMEM) (Invitrogen) supplemented with 10% heat inactivated Fetal Bovine Serum (FBS)
440 (Invitrogen), 10 mM (4-(2-hydroxyethyl)-1-piperazine ethanesulphonic acid) (HEPES) buffer
441 pH 7.2, 2 mM L-glutamine and 50 µg/ml of penicillin and streptomycin (Invitrogen). Cells were
442 incubated at 37°C in 5% CO₂. The *Toxoplasma* strains used in this study and listed in
443 [Supplementary Table 5](#) were maintained *in vitro* by serial passage on monolayers of HFFs. The
444 cultures were free of mycoplasma, as determined by qualitative PCR. *P. falciparum* parasites
445 were cultured using standard culture conditions. The drug sensitive laboratory strain 3D7 was
446 used in this study.

447

448 **Growth of *Cryptosporidium parvum* and RNA preparation.** Hct-8 cells were grown in a T-
449 75 flask (90% confluence) and infected with the *C. parvum* INRAE strain at a ratio of 5 oocysts
450 per cell. Altiratinib was added to the treated flask at a concentration of 500 nM concentration.
451 Four hours later, the flasks were washed to remove the oocysts and further incubated in presence
452 of altiratinib until 11h post infection. All cells were collected and RNA extracted in Trizol
453 solution for nanopore analyses.

454

455 ***In vitro* inhibition of *Eimeria tenella*.** Clec213 chicken epithelial cells were grown to sub-
456 confluence in P96-well plates and infected with *Eimeria tenella* sporozoites (INRAE strain)
457 expressing luciferase at a ratio of 1 sporozoite per cell. Four hours later, the plates were washed
458 and further incubated with different concentrations of altiratinib 44 hours after infection, when

459 luciferase activity was determined to quantify parasite development (six specimens were used
460 for each drug concentration).

461
462 **Medium-throughput screening.** The TargetMol (Boston, MA) compound library consists of
463 514 compounds (each as a 1 mM stock solution in DMSO). Primary screening was performed
464 in white 96-well plates (3610, Corning ® Costar ®). The confluent HFFs monolayer was
465 infected with 2000 RH NanoLuc parasites strain for 2 hours before the compounds were added
466 at a final concentration of 5 µM in a final volume of 100 µl. The culture was incubated at 37°C
467 for 48h. The medium was removed to add 50µl of PBS and measure the growth of the parasite
468 using the Nano-Glo® Luciferase Assay System, according to the manufacturer's instructions
469 (Promega). Lysis was performed in the wells by adding 50 µL of Nano-Glo® Luciferase Assay
470 Reagent with 1:50 dilution of Nano-Glo® Luciferase Assay Substrate. After 3 minutes of
471 incubation, luminescence was measured using the CLARIOstar® (BMG Labtech) plate reader.
472 The bioluminescence values of the uninfected host cells were used to determine the background
473 signal.

474
475 **Measurement of EC₅₀ for *Toxoplasma gondii* parasites.** To measure the EC₅₀ of *Toxoplasma*
476 *gondii* parasites, confluent HFFs monolayer was infected with 2000 tachyzoites of RH parasites
477 expressing the NLuc luciferase (RH NLuc) for 2h. After parasite invasion, each compound was
478 added to the culture in exponential concentrations. After 48h incubation at 37°C, the medium
479 was replaced with 50 µl of PBS. The reading of luminescence was performed using the Nano-
480 Glo® Luciferase Assay System according to the manufacturer's instructions (Promega). After
481 3 minutes of incubation, luminescence was measured using the CLARIOstar® (BMG Labtech)
482 plate reader. EC₅₀ values were determined using a non-linear regression analysis of normalized
483 data and assuming a sigmoidal dose response. EC₅₀ values for each compound represent the
484 average of three independent biological replicates. Statistical analyses were performed using
485 the one-way test ANOVA and GraphPad 8 software.

486
487 **Measurement of CC50 for mammalian cells and determination of Selectivity Index.**
488 Human HFFs, ARPE-19, MCF7, MDA-231 and U937 cell lines ([Supplementary Table 5](#)) were
489 plated for 1 hour in 96 well plates for 1h and incubated with exponential concentrations of the
490 indicated compounds in a final volume of 100 µl. After 72h of culture, CellTiter-Blue Reagent®
491 (Promega) (20 µl/well) was added directly to each well. Plates were then incubated at 37°C for
492 2 hours to allow cells to convert resazurin to resorufin before reading fluorescence (560(20))

493 Ex/ 590(10) Em) with the CLARIOstar® (BMG Labtech) plate reader. The cytotoxicity
494 concentration (CC₅₀) of human cells was determined using nonlinear regression curve of the
495 normalized data. CC₅₀ values represent the average of two biological experiments. The
496 Selectivity Index (SI) was determined by the average of the human CC₅₀ divided by the average
497 of the *T. gondii* EC₅₀. Mitochondrial toxicity assay was performed using the “Mitochondrial
498 ToxGlo™ Assay” kit according to the manufacturer's instructions (Promega). Briefly, 10,000
499 human cell lines were plated in 96 well plates with DMEM serum and glucose free,
500 supplemented with galactose (10 mM). After 3h of culture to allow cell adhesion, increasing
501 concentrations of altiratinib (tested drug) and sodium azide (positive control for mitochondrial
502 toxicity) or 800 µg/ml of digitonin (positive control for cell toxicity) were added. The cell
503 culture was maintained at 37°C for 90 min to detect cell viability (cytotoxicity) by fluorescence
504 and ATP production by luminescence using the CLARIOstar® (BMG Labtech) plate reader.

505

506 **Reagents.** The following primary antibodies were used in the immunofluorescence and
507 immunoblotting: rabbit anti-TgGAP45 (gift from Pr. Dominique Soldati, University of
508 Geneva), mouse anti-HA tag (Roche, RRID: AB_2314622), and rabbit anti-HA Tag (Cell
509 Signaling Technology, RRID: AB_1549585). Immunofluorescence secondary antibodies were
510 coupled with Alexa Fluor 488 or Alexa Fluor 594 (Thermo Fisher Scientific). Secondary
511 antibodies used in Western blotting were conjugated to alkaline phosphatase (Promega) or
512 horseradish peroxidase.

513

514 **Immunofluorescence microscopy.** *T. gondii* infecting HFF cells grown on coverslips were
515 fixed in 3% formaldehyde for 20 min at room temperature, permeabilized with 0.1% (v/v)
516 Triton X-100 for 15 min and blocked in Phosphate buffered saline (PBS) containing 3% (w/v)
517 BSA. The cells were then incubated for 1 hour with primary antibodies followed by the addition
518 of secondary antibodies conjugated to Alexa Fluor 488 or 594 (Molecular Probes). Nuclei were
519 stained for 10 min at room temperature with Hoechst 33258 at 2 µg/ mL in PBS. After four
520 washes in PBS, coverslips were mounted on a glass slide with Mowiol mounting medium, and
521 images were acquired with a fluorescence ZEISS ApoTome.2 microscope and images were
522 processed by ZEN software (Carl Zeiss, Inc.).

523

524 **Auxin induced degradation.** Depletion of TgPRP4K-AID-HA was achieved with 3-
525 Indoleacetic acid (IAA, Sigma-Aldrich # 45533) as described by Farhat *et al.*, 2020. A stock of
526 500 mM IAA dissolved in 100% EtOH at 1:1,000 was used to deplete mAID-tagged proteins

527 at a final concentration of 500 μ M. Mock treatment consisted of an equivalent volume of 100%
528 EtOH at a final concentration of 0.0789%, wt/vol. To monitor the degradation of AID-tagged
529 proteins, parasites grown in HFF monolayers were treated with auxin, or ethanol alone, for
530 different time intervals at 37°C. After treatment, parasites were harvested and analyzed by
531 immunofluorescence or Western blotting. Complete elimination of *TgPRP4K* parasites was
532 successful after 10 hours of IAA treatment.

533
534 **Plaque assays.** Confluent HFFs were infected with freshly egressed tachyzoites before adding
535 0.1% DMSO or the indicated compounds. Cultures were grown at 37°C for 7 days, fixed, and
536 stained with Coomassie blue staining solution (0.1% Coomassie R-250 in 40% ethanol and 10%
537 acetic acid). For cytotoxicity assay, the parasites were incubated with different drugs or DMSO
538 for 16 hours. After washing the cells, the cultures were left at 37°C for 3, 6 or 10 days before
539 fixation and staining. The size of the plaques when present was measured using ZEN 2 lite
540 software (Carl Zeiss, Inc.) and plotted using GraphPad Prism 8.

541
542 ***Toxoplasma gondii* genome editing.** Targeted genome modifications were performed using
543 the *T. gondii* adapted CRISPR/Cas9 system as previously described (Farhat *et al.*, 2020).
544 Recombinant parasites harboring allelic replacement for PRP4K^{F647S}, PRP4K^{L686F}, PRP4K^{L715F},
545 and PRP4K^{W649P} were generated by electroporation of the *T. gondii* RH NLuc strain with
546 pTOXO_Cas9CRISPR vectors targeting the *PRP4K* coding sequence (sgPRP4K^{F647S},
547 sgPRP4K^{L686F}, sgPRP4K^{L715F}) and their respective donor single-stranded oligo DNA
548 nucleotides (ssODNs) carrying respective nucleotide substitutions (PRP4K^{F647S}_donor,
549 PRP4K^{L686F}_donor, PRP4K^{L715F}_donor; Supplementary Table 5) for homology-directed repair.
550 Recombinant parasites were selected with 300nM altiratinib prior to subcloning by limited
551 dilution, and allelic replacement was verified by sequencing of *T. gondii TgPRP4K* genomic
552 DNA.

553
554 ***Toxoplasma gondii* random mutagenesis.** Parasites were chemically mutagenized as
555 previously described (Bellini *et al.*, 2020), with the following modifications. Briefly, $\sim 10^7$
556 tachyzoites growing intracellularly in HFF cells in a T25 flask were incubated for 4 h at 37°C
557 in 0.1% FBS DMEM growth medium containing either 2.5 mM ethyl methanesulphonate
558 (EMS) at final concentration or the appropriate vehicle controls. After exposure to the mutagen,
559 parasites were washed three times with PBS, and the mutagenized population was allowed to
560 recover in a fresh T25 flask containing an HFF monolayer in the absence of drug for 3–5 days.

561 The released tachyzoites were then inoculated into fresh cell monolayers in medium containing
562 300 nM of altiratinib and incubated until viable extracellular tachyzoites emerged 8–10 days
563 later. Surviving parasites were passaged once more under continued altiratinib treatment and
564 cloned by limiting dilution. The cloned mutants were each isolated from 6 independent
565 mutagenesis experiments. Thus, each flask contained unique SNV pools.

566

567 **RNA-seq, sequence alignment, and variant calling.** For each biological assay, a T175 flask
568 containing a confluent monolayer of HFF was infected with RH wild-type or Altiratinib-
569 resistant strains. Total RNAs were extracted and purified using TRIzol (Invitrogen, Carlsbad,
570 CA, USA) and RNeasy Plus Mini Kit (Qiagen). RNA quantity and quality were measured by
571 NanoDrop 2000 (Thermo Scientific). RNA-sequencing was performed as previously described
572 (Bellini *et al.*, 2020), following standard Illumina protocols, by GENEWIZ (South Plainfield,
573 NJ, USA). Briefly, the RNA quality was checked with the TapeStation System (Agilent
574 Technologies, Palo Alto, California, USA), and Illumina TruSEQ RNA library prep and
575 sequencing reagents were used following the manufacturer’s recommendations using polyA-
576 selected transcripts (Illumina, San Diego, CA, USA). The samples were paired-end multiplex
577 sequenced (2 x 150 bp) on the Illumina HiSeq 2500 platform and generated at least 40 million
578 reads for each sample. The quality of the raw sequencing reads was assessed using FastQC
579 (<http://www.bioinformatics.babraham.ac.uk/projects/fastqc/>) and MultiQC (Ewels et al., 2016).
580 The RNA-Seq reads (FASTQ) were processed and analyzed using the Lasergene Genomics
581 Suite version 17 (DNASTAR, Madison, WI, USA) using default parameters. The paired-end
582 reads were uploaded onto the SeqMan NGen (version 17, DNASTAR, Madison, WI, USA)
583 platform for reference-based assembly and variant calling using the *Toxoplasma* Type I GT1
584 strain (ToxoDB-46, GT1 genome) as reference template. The ArrayStar module (version 17,
585 DNASTAR, Madison, WI, USA) was used for variant detection and statistical analysis of
586 uniquely mapped paired-end reads using the default parameters. Variant calls were filtered to
587 select variants present in coding regions with the following criteria: variant depth ≥ 30 , Q call
588 ≥ 60 , and absent in the parental wild-type strain. Mutations were plotted on a Circos plot using
589 Circa (OMGenomics.com). For the expression data quantification and normalization, the
590 FASTQ reads were aligned in parallel to the ToxoDB-46 build of the *Toxoplasma gondii* GT1
591 genome (ToxoDB-46) using Subread version 2.0.1 (Liao et al., 2013) with the following options
592 ‘subread-align -d 50 -D 600 --sortReadsByCoordinates’. Read counts for each gene were
593 calculated using featureCounts from the Subread package. Differential expression analysis was

594 conducted using DESeq2 and default settings within the iDEP.92 web interface. Transcripts
595 were quantified and normalized using TPMCalculator.

596

597 **Plasmid construction.** The plasmids and primers for gene of interest (GOI) used in this work
598 are listed in [Supplementary Table 5](#). To construct the vector pLIC-GOI-HAFlag, the coding
599 sequence of GOI was amplified using primers LIC-GOI-Fwd and LIC-GOI-Rev using *T. gondii*
600 genomic DNA as template. The resulting PCR product was cloned into the pLIC-HF-dhfr or
601 pLIC-mCherry-dhfr vectors using the Ligation Independent Cloning (LIC) cloning method.
602 Twenty mers-oligonucleotides corresponding to specific GOI were cloned using Golden Gate
603 strategy. Briefly, primers GOI-gRNA-Fwd and GOI-gRNA-Rev containing the sgRNA
604 targeting GOI genomic sequence were phosphorylated, annealed and ligated into the
605 pTOXO_Cas9-CRISPR plasmid linearized with BsaI, leading to pTOXO_Cas9-
606 CRISPR::sgGOI. Just two transgenic components are needed to implement the auxin-inducible
607 degron (AID) system, a plant auxin receptor called transport inhibitor response 1 (TIR1) and a
608 POI tagged with an AID. We engineered a type I RH Δ ku80 and a type II lines of *T. gondii* to
609 stably express Tir1 from *Oryza sativa* tagged with Ty and controlled by a promoter selected for
610 a moderate expression of the chimeric protein. The plasmid *pModProm1-TiR1-TY1-3DHFR*
611 (DNA sequence in [Supplementary Table 5](#) was DNA synthesized and then cloned in pUC57
612 simple by Genscript. The chimeric construct was inserted within the UPRT locus. We also
613 created a pLIC vector containing a codon-optimized for *T. gondii* expression DNA block with
614 the mAID from *Arabidopsis thaliana* auxin-responsive protein IAA17^{E66-S133}, as defined in
615 [Farhat et al., 2020](#), in frame with a HA tag ([Supplementary Table 5](#)).

616

617 ***Toxoplasma gondii* transfection.** *T. gondii* strains were electroporated with vectors in cytomix
618 buffer (120 mM KCl, 0.15 mM CaCl₂, 10 mM K₂HPO₄/ KH₂PO₄ pH 7.6, 25 mM HEPES pH7.6,
619 2 mM EGTA, 5 mM MgCl₂) using a BTX ECM 630 machine (Harvard Apparatus).
620 Electroporation was performed in a 2 mm cuvette at 1.100V, 25 Ω and 25 μ F. When needed,
621 the antibiotic (concentration) used for drug selection was chloramphenicol (20 μ M),
622 mycophenolic acid (25 μ g/ml) with xanthine (50 μ g/ml), pyrimethamine (3 μ M), or 5-
623 fluorodeoxyuracil (10 μ M). Stable transgenic parasites were selected with the appropriate
624 antibiotic, single-cloned in 96 well plates by limiting dilution and verified by
625 immunofluorescence assay or genomic analysis.

626

627 **Chromatographic purification of *TgPRP4K*- and *TgPRP8*-containing complex.** *T. gondii*
628 extracts from RH $\Delta ku80$ or Pru $\Delta ku80$ cells stably expressing HAFlag-tagged *TgPRP4K* and
629 *TgPRP8*, were incubated with anti-FLAG M2 affinity gel (Sigma-Aldrich) for 1 hour at 4°C.
630 Beads were washed with 10-column volumes of BC500 buffer (20 mM Tris-HCl, pH 8.0, 500
631 mM KCl, 20% glycerol, 1 mM EDTA, 1 mM DTT, 0.5% NP-40, and protease inhibitors).
632 Bound polypeptides were eluted stepwise with 250 μ g/ml FLAG peptide (Sigma Aldrich)
633 diluted in BC100 buffer. For size-exclusion chromatography, protein eluates were loaded onto
634 a Superose 6 HR 10/30 column equilibrated with BC500. Flow rate was fixed at 0.35 ml/min,
635 and 0.5-ml fractions were collected.

636

637 **Mass spectrometry-based Interactome analyses.** Protein were stained with colloidal blue
638 (Thermo Fisher Scientific) and gel bands excised before in-gel digestion using modified trypsin
639 (Promega, sequencing grade). Resulting peptides were analyzed by online nanoliquid
640 chromatography coupled to tandem MS (UltiMate 3000 RSLCnano and Q-Exactive HF,
641 Thermo Scientific). Peptides were sampled on a 300 μ m x 5 mm PepMap C18 precolumn and
642 separated on a 75 μ m x 250 mm C18 column (Reprosil-Pur 120 C18-AQ, 1.9 μ m, Dr. Maisch)
643 using 50-min gradients. MS and MS/MS data were acquired using Xcalibur (Thermo
644 Scientific). Peptides and proteins were identified using Mascot (version 2.6) through
645 concomitant searches against the *Toxoplasma gondii* database (ME49 taxonomy, version 30
646 downloaded from ToxoDB⁴⁷, the Uniprot database (*Homo sapiens* taxonomy, February 2019
647 download), a homemade database containing the sequences of classical contaminants, and the
648 corresponding reversed databases. Trypsin was chosen as the enzyme and two missed cleavages
649 were allowed. Precursor and fragment mass error tolerances were set at respectively 10 ppm
650 and 25 mmu. Peptide modifications allowed during the search were: Carbamidomethyl (C,
651 fixed), Acetyl (Protein N-term, variable) and Oxidation (M, variable). The Proline software
652 (<http://proline.profiroteomics.fr>) was used to filter the results: conservation of rank 1 peptide-
653 spectrum-matches (PSMs), PSM homology threshold p -value ≤ 0.01 , PSM score ≥ 25 , and
654 minimum of 1 specific peptide per identified protein group. Proline was then used to perform a
655 compilation and grouping of the protein groups identified in the different samples. The MS data
656 have been deposited to the ProteomeXchange Consortium via the PRIDE partner repository
657 with the dataset identifier [PXD029455](https://proteomecentral.proteomexchange.org/datasets/PXD029455) and [10.6019/PXD029455](https://proteomecentral.proteomexchange.org/datasets/10.6019/PXD029455). Proteins from the
658 contaminant database were discarded from the final list of identified proteins. MS1-based label
659 free quantification of the protein groups was performed using Proline to infer intensity-based

660 absolute quantification (iBAQ) values that were used to rank identified *Toxoplasma* proteins in
661 the interactomes.

662

663 **Gene synthesis for recombinant expression of *TgPRP4K* and *PfCLK3*.** Gene synthesis for
664 all insect cell codon optimized constructs was provided by Genscript. The original *T. gondii*
665 *TgPRP4K* construct (aa 534-895) or *PfCLK3* (aa 336-692) were designed with non-cleavable
666 C-terminal 6His tags and cloned between BamHI and HindIII sites into the pFastBac1 vector
667 (Invitrogen). Point mutation variations of this initial construct were subsequently modified by
668 Genscript from this original template. For the crystallization of *TgPRP4K*, the cysteine 573 was
669 mutated to a serine to prevent the formation of homomeric disulfide bond.

670

671 **Generation of baculovirus.** Bacmid cloning steps and baculovirus generation were performed
672 using EMBacY baculovirus ([kindly gifted by Imre Berger](#)), which contains a YFP reporter gene
673 in the virus backbone. The established standard cloning and transfection protocols setup within
674 the EMBL Grenoble eukaryotic expression facility were used. While baculovirus synthesis
675 (V0) and amplification (to V1) were performed with SF21 cells cultured in SF900 III media
676 (Life Technologies), large-scale expression cultures were performed with Hi-5 cells cultured in
677 Express-Five media (Life Technologies) and infected with 0,5% vol/vol of generation 2 (V1)
678 baculovirus suspensions and harvested 72h post-infection.

679

680 **Protein expression and purification.** For purification, 3 cell pellets of approximately 800 mL
681 of Hi-5 culture were each resuspended in 50 mL of lysis buffer (50 mM Tris pH 8.0, 500 mM
682 NaCl and 4 mM β -mercaptoethanol (β -ME)) in the presence of an anti-protease cocktail
683 (Complete EDTA free, Roche) and 1 ul benzonase (MERK Millipore 70746). Lysis was
684 performed on ice by sonication for 3 min (30 sec on/ 30 sec off, 45° amplitude). After the lysis
685 step, 5% of glycerol was added. Clarification was then performed by centrifugation for 1h at
686 12,000 xg and 4°C. After that, 20 mM imidazole was added to the supernatant and incubated
687 with 5 mL of Ni-NTA resin (Qiagen) with a stirring magnet at 4°C for 30 min. All further
688 purification steps were then performed at room temperature. After flowing through the lysate,
689 the resin was washed with 10 column volumes of lysis buffer containing 20 mM imidazole.
690 Elution was then performed by increasing the imidazole content to 300 mM in a buffer system
691 containing 200 mM NaCl, 50 mM Tris pH 7.5, 2 mM BME and 5% glycerol. Eluted fractions
692 were pooled based on an SDS PAGE gel analysis and flown directly through a previously
693 equilibrated (in 200 mM NaCl, 50 mM Tris pH 7.5, 2 mM BME and 5% glycerol) heparin

694 column connected to an AKTA© pure system. After a 10 cv wash, the heparin was eluted using
695 a 40 mL gradient reaching 2M NaCl. Finally, the sample was injected onto a SUPERDEX 200
696 increase 10/300GL (GE Healthcare) column running in 50 mM Tris pH: 7.5, 250 mM NaCl, 1
697 mM BME and 1% glycerol and the elution was monitored at 280 nm. Peak fractions were
698 concentrated using a 30 kDa Amicon ultra (Sigma Aldrich) concentrator before being frozen in
699 liquid nitrogen and stored long-term at -80°C.

700

701 **Western blot.** Immunoblot analysis of protein was performed as described in [Farhat *et al.*,](#)
702 [2020](#). Briefly, $\sim 10^7$ cells were lysed in 50 μ l lysis buffer (10 mM Tris-HCl, pH6.8, 0.5 % SDS
703 [v/v], 10% glycerol [v/v], 1 mM EDTA and protease inhibitors cocktail) and sonicated. Proteins
704 were separated by SDS-PAGE, transferred to a polyvinylidene fluoride membrane (Immobilon-
705 P; EMD Millipore) by liquid transfer, and Western blots were probed using appropriate primary
706 antibodies followed by alkaline phosphatase or horseradish peroxidase-conjugated goat
707 secondary antibodies. Signals were detected using NBT-BCIP (Amresco) or enhanced
708 chemiluminescence system (Thermo Scientific).

709

710 **Thermal Shift Assay (TSA).** The thermal stability of recombinant WT and mutants *TgPRP4K*
711 proteins in the presence or absence of altiratinib compound was performed in TSA buffer (400
712 mM NaCl, 50 mM Hepes, 1 mM MgCl₂ and 2 mM beta-mercaptoethanol). Each assay tube
713 contained a reaction mixture (final volume of 20 μ l) of recombinant PRP4K enzyme (0.170
714 mg/ml) and 100 μ M inhibitor or 1% dimethyl sulfoxide (DMSO) in TSA buffer. The reactions
715 were incubated at increasing temperatures, 30°C, 33°C, 36 C°, 39°C, 42°C, 45°C, 48°C, 51°C,
716 54°C, 57°C, 60°C, 63°C, 66°C, 69°C, for 3 minutes and then centrifuged at 16000 xg for 25
717 minutes. The supernatant was collected to verify the presence of the recombinant PRP4K/CLK3
718 proteins by Western blot. Proteins were blotted as previously described and detected using Anti-
719 polyHistidine-Peroxidase monoclonal antibody (Sigma-Aldrich # A7058) and signals were
720 revealed using the Metal Enhanced DAB Substrate Kit, according to the manufacturer's
721 instructions (Thermo Scientific # 34065).

722

723 **Microscale thermophoresis (MST).** MST measurements were performed using a
724 NanoTemper Monolith NT.115 Green/Red instrument (NanoTemper Technologies). *TgPRP4K*
725 protein was labeled using the Monolith His-Tag Labeling Kit RED-tris-NTA 2nd Generation
726 (NanoTemper Technologies). The labeled *TgPRP4K* protein was adjusted to 100 nM with a
727 buffer containing 30 mM Hepes (PH 7.5), 400 mM NaCl, 2% Glycerol, 0.5 mM beta-

728 mercaptoethanol. A series of 16 1:1 dilutions of the ligands was prepared using the same buffer.
729 Subsequently, each ligand dilution was mixed with 1 volume of the labeled *TgPRP4K* protein.
730 Samples were placed in Premium capillaries (NanoTemper technologies) for measurements.
731 Instrument parameters were set to 40% LED power and 40% MST power. Data from three
732 independently pipetted measurements were analyzed with MO. Affinity Analysis software
733 (NanoTemper Technologies) using the signal from an MST-on time at 1.5 sec after T-jump.

734
735 **SEC-MALLS.** All MALLS runs were performed using an S200 Increase SEC column
736 (10/300 GL, GE Healthcare). Sample injection and buffer flow were controlled by a Hitachi
737 L2130 pump. The SEC column was followed by an L-2400 UV detector (Hitachi), an Optilab
738 T-rEX refractometer (Wyatt technologies), and a DAWN HELEOS-II multi-angle light
739 scattering detector (Wyatt technologies). Injections of 50 μL were performed using protein
740 samples concentrated at a minimum of 4 $\text{mg}\cdot\text{mL}^{-1}$, a constant flow rate of 0.5 $\text{mL}\cdot\text{min}^{-1}$ was
741 used. Accurate MALLS mass prediction was performed with the Astra software (Wyatt
742 Technologies). The curves were plotted using Graphpad (Prism).

743 **Crystallization with Altiratinib.** For *TgPRP4K*/Altiratinib co-crystal growth, *TgPRP4K* at 2-
744 5 mg/ml was incubated for 20 minutes with 400 μM of altiratinib prior to injection on an S200
745 column running 50 mM Tris pH 7.5, 250 mM NaCl, 1 mM B-ME and 1% glycerol. The eluted
746 protein was then pooled and concentrated to 20 mg/ml . It should be noted that altiratinib
747 generates a typical absorbance signature below 260 nm which increases with the concentration
748 of the protein. Crystallization was setup using the hanging drop vapor diffusion method with
749 *TgPRP4K*/altiratinib mixed in a 1/1 ratio with 18% PEG 3350 and 0.18 M Potassium
750 thiocyanate. Crystals appeared generally after 2 weeks. The crystals were harvested using
751 Hampton nylon loops, cryo-protected in the mother liquor supplemented with 18-20% glycerol
752 and flash frozen in liquid nitrogen.

753 **Data collection and structure determination.** X-ray diffraction data for *TgPRP4k*/altiratinib
754 crystals were collected by the autonomous beamline MASSIF-1 at the European Synchrotron
755 Radiation Facility (ESRF) beamline MASSIF-1 (Bowler et al., 2015; Svensson et al., 2015)
756 using automatic protocols for the location and optimal centering of crystals (Svensson et al.,
757 2018). Strategy calculations accounted for flux and crystal volume in the parameter prediction
758 for complete datasets. Diffraction was performed at 100K. Data collection was performed using
759 XDS (Kabsch, 2010) while amplitude scaling/merging was handled by the Staraniso server
760 (Global phasing LTD). Molecular replacement solutions were obtained with Phaser (McCoy et

761 *al.*, 2007) (within Phenix) using the crystal structure of human PRPF4B bound to rebastinib
762 [Protein Data Bank (PDB) code: 6CNH] as a template, the initial solution was then improved
763 through cycles of manual adjustment in Coot (Emsley and Cowtan, 2004) and automated
764 building in phenix autobuild (Terwilliger et al., 2008). The Altiratinib geometry restraints were
765 generated in phenix using *elbow*. Refinement was performed using Refmac5, phenix resolve or
766 Buster (Global Phasing Ltd). Final pdb model corrections were performed using the pdb-redo
767 server.

768 **Structure representations.** Structural representations of *Tg*PRP4K and *Pf*PRP4K/CLK3 were
769 performed using UCSF-Chimera while the schematic representation of altiratinib interaction
770 network was computed using Ligplot.

771 **Direct RNA sequencing by nanopore.** The mRNA library preparation followed the SQK-
772 RNA002 kit (Oxford Nanopore) recommended protocol, the only modification was the input
773 mRNA quantity increased from 500 to 1000 ng, all other consumables and parameters were
774 standard. Final yields were evaluated using the Qubit HS dsDNA kit (Thermofisher Q32851)
775 with minimum RNA preps reaching at least 150 ng. For all conditions, sequencing was
776 performed on FLO-MIN106 flow cells either using a MinION MK1C or MinION sequencer.
777 All datasets were subsequently basecalled with a Guppy version higher than 5.0.1 with a
778 Qscore cutoff > 7. Long read alignment were performed by Minimap2 as previously described
779 (Farhat et al., 2021). Alignments were converted and sorted using samtools.

780 **Differential splicing analysis.** Splice correction, collapse, quantification and differential
781 isoform representation was performed using the FLAIR pipeline (Tang et al., 2020) with
782 standard parameters however keeping non-consistent isoforms after the correction stage. The
783 difference splicing script was used to generate gtf track files and quantification histograms.

784 **Intron retention quantification.** Prior to counting retained introns the original gff files from
785 eupadDB were processed using the Agat-conv (<https://github.com/NBISweden/AGAT>)
786 program “agat_convert_sp_gff2gtf.pl”. Introns were added to the gtf file with
787 “agat_sp_add_introns.pl”. A per transcript intron retention ratio was calculated by counting per
788 transcript intron counts divided by standard transcript counts (+1) using htseq-count with the
789 following input parameters parameters:

790 • “htseq-count -f bam -r name -s yes -i Parent -t intron -m intersection-nonempty” for
791 retained introns per-transcript

792 • “htseq-count -f bam -r name -s yes -i ID -t transcript -m intersection-nonempty” for total
793 transcripts

794 Subsequent merging treatment of count data was carried out in excel worksheets. The intron
795 retention analysis was limited to spliced genes with a minimum of 2 transcripts. Intron retention
796 values above 1 were excluded as these values are probably the consequence of mis-annotated
797 genes. Final distributions of retained intron ratios were done in GraphPad Prism.

798
799 **Software and Statistical analyses.** Volcano plots, scatter plots, and histograms were generated
800 with Prism 7. Sample sizes were not predetermined and chosen according to previous literature.
801 All experiments were performed in biological replicates to allow for statistical analyses. No
802 method of randomization was used. All experiments were performed in independent biological
803 replicates as stated for each experiment in the manuscript. All corresponding treatment and
804 control samples from RNA-seq were processed at the same time to minimize technical
805 variation. Investigators were not blinded during the experiments. Experiments were performed
806 in biological replicates and provided consistent statistically relevant results.

807
808 ***P. falciparum* EC50 determination.** EC50 values were obtained as previously described
809 (Nardella F *et al.*, 2020). Briefly, a range of 2-step serial dilutions of altiratinib (starting
810 concentration 5 μ M) and Dihydroartemisinin (DHA, starting concentration 50 nM) were used
811 to assess the activity of the compounds. GraphPad Prism 8 was used to interpolate IC₅₀ from
812 three independent experiments run in triplicate. DHA and DMSO were used as positive and
813 negative controls, respectively.

814
815 ***P. falciparum* treatment and harvesting for RNA extraction.** 3.10⁹ trophozoite-stage
816 parasites aged of 24- to 30-hours post-red blood cell invasion were treated for 8 hours with a
817 concentration of 2.5 μ M of altiratinib (corresponding to the EC₉₀) or 0.1% DMSO (vehicle).
818 The concentration and incubation time chosen were checked previously for inducing no obvious
819 growth phenotype. Parasites were then washed with RPMI (Gibco) and harvested using 0.15%
820 saponin lysis of the surrounding red blood cell. After thorough washing with PBS, RNA was
821 extracted using the RNeasy mini kit (Qiagen) and sent for analysis. RNA was harvested in two
822 independent experiments.

823

824 **Data availability**

825 Correspondence and requests for materials should be addressed to M.A.H. The Nanopore
826 RNAseq data have been deposited in NCBI's SRA data [PRJNA774463](https://www.ncbi.nlm.nih.gov/sra/PRJNA774463). The coordinates and
827 structure factors for the *Tg*PRP4k/altiratinib structure have been deposited in the PDB with the
828 accession number [7Q4A](https://www.rcsb.org/structure/7Q4A). The mass spectrometry proteomics data were deposited with the
829 ProteomeXchange Consortium via the PRIDE partner repository with the record identifier :
830 [pxd029455](https://proteomecentral.proteomex.org/pride/pxd029455).

831

832 **Acknowledgments**

833 This work was supported by the Laboratoire d'Excellence (LabEx) ParaFrap [ANR-11-LABX-
834 0024], the Agence Nationale pour la Recherche [Project HostQuest, ANR-18-CE15-0023,
835 Project ApiNewDrug, ANR-21-CE35-0010-01, Project EpiKillMal, ANR-20-CE18-0006], the
836 European Research Council [ERC Consolidator Grant N°614880 Hosting TOXO to M.A.H.],
837 and Fondation pour la Recherche Médicale [FRM Equipe # EQU202103012571] and Roux-
838 Cantarini Fellowship attributed to FN. The proteomic experiments were partially supported by
839 Agence Nationale de la Recherche under projects ProFI (Proteomics French Infrastructure,
840 ANR-10-INBS-08) and GRAL, a program from the Chemistry Biology Health (CBH) Graduate
841 School of University Grenoble Alpes (ANR-17-EURE-0003). The HTX Lab (EMBL Grenoble)
842 are thanked for support in screening for crystal conditions and automatic mounting of crystals.

843

844 **Author Contributions**

845 MAH led the research and coordinated the collaboration. MAH, AB and CS designed the
846 project. CS, VB, MWB, FN, MPBP, CM, DC, YC, LB, FL, AB, AS and MAH designed,
847 conducted and interpreted the experimental work. M.-A.H., A.B. and C.S. wrote the paper with
848 editorial assistance from VB and fruitful comments from all other authors.

849

850 **Declaration of Interests**

851 The authors declare no competing interests.

852

853 **References**

- 854 1. De Rycker, M. et al. Challenges and recent progress in drug discovery for tropical
855 diseases. *Nature* 559, 498–506 (2018).
- 856 2. Montoya, JG., & Liesenfeld, O. Toxoplasmosis. *Lancet* 363, 1965–1976 (2004).

- 857 3. Dunay, I.R. et al. Treatment of toxoplasmosis: historical perspective, animal models,
858 and current clinical practice. *Clin. Microbiol. Rev.* 31, e00057-17 (2018).
- 859 4. Kwon, Y. et al. Effective inhibition of c-MET-mediated signaling, growth and migration
860 of ovarian cancer cells is influenced by the ovarian tissue microenvironment. *Oncogene*
861 34, 144–153 (2015).
- 862 5. Smith, DB et al. Altiratinib Inhibits Tumor Growth, Invasion, Angiogenesis, and
863 Microenvironment-Mediated Drug Resistance via Balanced Inhibition of MET, TIE2,
864 and VEGFR2. *Mol Cancer Ther.* 9, 2023-2034 (2015).
- 865 6. Alam, M.M. et al. Validation of the protein kinase Pf CLK3 as a multistage cross-
866 species malarial drug target *Science* 365(6456):eaau1682 (2019).
- 867 7. Mahindra, A. et al., Development of Potent PfCLK3 Inhibitors Based on TCMDC-
868 135051 as a New Class of Antimalarials. *J Med Chem.* 2020 63, 9300-9315 (2020).
- 869 8. Schneider, M. et al. Human PRP4 kinase is required for stable tri-snRNP association
870 during spliceosomal B complex formation. *Nat Struct Mol Biol.* 17, 216-21 (2010).
- 871 9. Lützelberger, M., & Käufer, N.F. The Prp4 Kinase: Its Substrates, Function and
872 Regulation in Pre-mRNA Splicing. In: Dr. Huang Cai (Ed.), editor. *Protein*
873 *Phosphorylation in Human Health: InTech.* (2012).
- 874 10. Corkery, D.P. et al. Connecting the speckles: Splicing kinases and their role in
875 tumorigenesis and treatment response. *Nucleus* 6, 279-88 (2015).
- 876 11. Eckert, D. et al. Prp4 Kinase Grants the License to Splice: Control of Weak Splice Sites
877 during Spliceosome Activation. *PLoS Genet.* 12, e1005768 (2016).
- 878 12. Bellini, V. et al. Target Identification of an Antimalarial Oxaborole Identifies AN13762
879 as an Alternative Chemotype for Targeting CPSF3 in Apicomplexan Parasites. *iScience.*
880 23, 101871 (2020).
- 881 13. Talevich, E. et al. Structural and evolutionary divergence of eukaryotic protein kinases
882 in Apicomplexa. *BMC Evol. Biol.* 11, 321 (2011).
- 883 14. Zhou, Z. & Fu, X. D. Regulation of splicing by SR proteins and SR protein-specific
884 kinases. *Chromosoma* 122, 191–207 (2013).
- 885 15. Agarwal, S. et al. Two nucleus-localized CDK-like kinases with crucial roles for
886 malaria parasite erythrocytic replication are involved in phosphorylation of splicing
887 factor. *J. Cell. Biochem.* 112, 1295–1310 (2011).
- 888 16. Sidik, S.M. et al. A Genome-wide CRISPR Screen in Toxoplasma Identifies Essential
889 Apicomplexan Genes. *Cell.* 166, 1423-1435 (2016).

- 890 17. Lee VV et al. Identification and characterisation of splicing regulators in *Toxoplasma*
891 *gondii*. <https://www.biorxiv.org/content/10.1101/2021.06.27.450092v3>
- 892 18. Bottner, C.A. et al. Multiple genetic and biochemical interactions of Brr2, Prp8, Prp31,
893 Prp1 and Prp4 kinase suggest a function in the control of the activation of spliceosomes
894 in *Schizosaccharomyces pombe*. *Curr Genet.* 48, 151-61 (2005).
- 895 19. Charenton, C. et al. Mechanism of 5' splice site transfer for human spliceosome
896 activation. *Science.* 364, 362-367 (2019).
- 897 20. Bertram, K. et al. Cryo-EM Structure of a Pre-catalytic Human Spliceosome Primed for
898 Activation. *Cell* 170, 701–713 (2017).
- 899 21. Dellaire, G. et al. Mammalian PRP4 kinase copurifies and interacts with components of
900 both the U5 snRNP and the N-CoR deacetylase complexes. *Mol Cell Biol.* 22, 5141-
901 5156 (2002).
- 902 22. Greene, E.A., et al. Spectrum of chemically induced mutations from a large-scale
903 reverse-genetic screen in *Arabidopsis*. *Genetics* 164, 731–740 (2003).
- 904 23. Schneider, M. et al. Human PRP4 kinase is required for stable tri-snRNP association
905 during spliceosomal B complex formation. *Nat. Struct. Mol. Biol.* 17, 216–221 (2010).
- 906 24. Tang, A.D. et al. Full-length transcript characterization of SF3B1 mutation in chronic
907 lymphocytic leukemia reveals downregulation of retained introns. *Nat Commun.* 11,
908 1438 (2020).
- 909 25. Oesterreich, F.C. et al. Splicing of nascent RNA coincides with intron exit from RNA
910 polymerase II. *Cell*, 165, 372–381 (2016)
- 911 26. Herzel, L., et al. Long-read sequencing of nascent RNA reveals coupling among RNA
912 processing events. *Genome Res.*, 28, 1008–1019 (2018).
- 913 27. Jumper J, et al. Highly accurate protein structure prediction with AlphaFold. *Nature.*
914 596, 583-589 (2021).
- 915 28. Mirdita, M. et al. ColabFold - Making protein folding accessible to all.
916 <https://www.biorxiv.org/content/10.1101/2021.08.15.456425v1> (2021).
- 917 29. Artim, S.C. et al. Assessing the range of kinase autoinhibition mechanisms in the insulin
918 receptor family. *Biochem J.* 448, 213-220 (2012).
- 919 30. Mendrola, J.M. et al. Receptor tyrosine kinases with intracellular pseudokinase
920 domains. *Biochem Soc Trans.* 41, 1029-1036 (2013).
- 921 31. Schneider, M. et al. Human PRP4 kinase is required for stable tri-snRNP association
922 during spliceosomal B complex formation. *Nat Struct Mol Biol.* 17, 216-221 (2010).

- 923 32. Farhat, D.C. et al. A MORC-driven transcriptional switch controls *Toxoplasma*
924 developmental trajectories and sexual commitment. *Nat Microbiol.* 5, 570-583 (2020).
- 925 33. Bowler, M.W. et al. MASSIF-1: a beamline dedicated to the fully automatic
926 characterization and data collection from crystals of biological macromolecules. *Journal*
927 *of Synchrotron Radiation* 22:1540–1547 (2015).
- 928 34. Svensson, O. et al. Fully automatic characterization and data collection from crystals of
929 biological macromolecules. *Acta crystallographica. Section D, Biological*
930 *crystallography* 71:1757–1767 (2015).
- 931 35. Svensson, O. et al. Multi-position data collection and dynamic beam sizing: recent
932 improvements to the automatic data-collection algorithms on MASSIF-1. *Acta*
933 *Crystallographica Section D Structural Biology* 74:433–440 (2018).
- 934 36. Kabsch W. XDS. *Acta crystallographica. Section D, Biological crystallography* 66:125–
935 132 (2010).
- 936 37. McCoy, A.J. et al. Phaser crystallographic software. *Journal of applied crystallography*
937 40:658–674 (2007).
- 938 38. Emsley, P. & Cowtan, K. Coot: model-building tools for molecular graphics. *Acta*
939 *crystallographica. Section D, Biological crystallography* 60:2126–2132 (2004).
- 940 39. Terwilliger, T.C., et al. Iterative model building, structure refinement and density
941 modification with the PHENIX AutoBuild wizard. *Acta crystallographica. Section D,*
942 *Biological crystallography* 64:61–69 (2008).
- 943 40. Farhat, D. C. et al. A plant-like mechanism coupling m6A reading to polyadenylation
944 safeguards transcriptome integrity and developmental gene partitioning in *Toxoplasma*.
945 *Elife.* 10:e68312 (2021).
- 946 41. Nardella, F. et al. DNA Methylation Bisubstrate Inhibitors Are Fast-Acting Drugs
947 Active against Artemisinin-Resistant *Plasmodium falciparum* Parasites. *ACS Cent Sci.*
948 6:16-21 (2020).
- 949
950
951
952
953
954
955
956

957 **Figure Legends**

958 **Fig. 1 | Efficacy of altiratinib against the parasite *Toxoplasma gondii*.** **a**, Graphical
959 representation of data from the medium-throughput screen. A cutoff was set at 70% of parasite
960 inhibition. Red dots, hits. The workflow used for the screening is shown in **Extended Data Fig.**
961 **1a. b**, The half-maximal effective concentration (EC₅₀) values of the 14 molecules validated at
962 1 μM. **c**, Chemical structure of altiratinib. **d**, EC₅₀ values for pyrimethamine and altiratinib. The
963 confluent HFF monolayer was infected with tachyzoites of the *T. gondii* RH_NanoLucEmGFP
964 strain (**Supplementary Table 5**). The EC₅₀ values of each biological replicate were determined
965 by non-linear regression analysis. EC₅₀ data are presented as mean \pm SD from 3 independent
966 biological replicates, each with 3 technical replicates. **e**, Compound efficiency presented by
967 IFA. Confluent HFFs were infected with *T. gondii* RH_NanoLucEmGFP and incubated with
968 1 μM of pyrimethamine, 300 nM of altiratinib or 0.1% of the vehicle (DMSO) for 24h. Fixed
969 cells were stained with anti-inner membrane complex protein (GAP45) antibody (magenta). In
970 green the cytosolic GFP. Scale bar corresponds to 5 μm. **f**, Dose-response curves of HFFs,
971 ARPE-19, MCF7, MDA231 and U937 cell lines in the presence of altiratinib. Human cells were
972 plated out and incubated with increasing concentrations of the drug. After 72h, cell viability
973 was determined using the “*CellTiter-Blue Assay*” kit (Promega) and cell cytotoxicity
974 concentration (CC50) was calculated. The graph is representative of two different experiments
975 performed in triplicate. The shaded error envelopes indicate 95% confidence intervals. On the
976 right, CC50 values show the mean of two experiments. Selectivity index (SI) is based on the
977 average of human CC50 divided by the average of *T. gondii* EC50. **g**, Effect concentration
978 curve of *Eimeria tenella* in presence of altiratinib. **h**, Altiratinib inhibition of *Neospora caninum*
979 proliferation shown by plaque assay. After 7 days of infection and drugs incubation, the size of
980 at least 50 plaques were measured. n.d., not detected. **i**, Dose-response curves of altiratinib and
981 dihydroartemisinin (DHA) in *P. falciparum* asexual blood-stage. Graph is representing the
982 mean and SD values obtained in three independent experiments run in triplicate.

983
984 **Fig. 2 | Deconvolution and validation of the *TgPRP4K* molecular target.** **a**, Circos plot
985 summarizing the single nucleotide variants (SNVs) detected by transcriptomic analysis of *T.*
986 *gondii* altiratinib -resistant lines, grouped by chromosome (numbered in Roman numerals with
987 size intervals indicated on the outside). Each dot in the six innermost gray tracks corresponds
988 to a scatter plot of the mutations identified in the six drug-resistant strains, with each ring
989 representing one of the six drug-resistant lines (A through F). Each bar in the outermost track

990 represents the positions of selected archetypal essential genes. See [Supplementary Table 2](#) for
991 transcriptomic analysis. **b**, Schematic representation of the *TgPRP4K* protein structure. The
992 kinase domain is predicted in the C-terminal portion of the protein. Phosphorylated and
993 acetylated residues are shown as blue and red dots, respectively. The orange dots correspond to
994 the three discovered SNVs located in the kinase domain. **c**, The nuclear location of *TgPRP4K*
995 (red) in human primary fibroblasts (HFFs) infected with parasites expressing an HA–Flag-
996 tagged copy of *TgPRP4K*. Cells were co-stained with Hoechst DNA-specific dye (blue) and the
997 anti-Inner Membrane Complex (IMC) (green) antibody. Scale bar, 5 μ m. **d**, Graphs representing
998 the essentiality of *TgPRP4K* protein assessed by plaque assay. RH_Tir1-Ty and *TgPRP4K* KD
999 parasites were either untreated or treated with IAA for 7 days and the size of 42 plaques were
1000 measured upon detection. n.d., not detected. **e**, Fluorescence microscopy showing intracellular
1001 growth of WT and the *TgPRP4K* edited parasites (F647S, L686F, L715F). HFF cells were
1002 infected with tachyzoites of the indicated *T. gondii* strains expressing the NLuc-P2A-EmGFP
1003 reporter gene and incubated with 300 nM of altiratinib or 0.1% DMSO as control. Cells were
1004 fixed 24 h post-infection and then stained with antibodies against the *T. gondii* inner membrane
1005 complex protein GAP45 (magenta). The cytosolic GFP is shown in green. Scale bars represent
1006 5 μ m. **f**, EC₅₀ values for pyrimethamine (Pyr) and altiratinib were determined for WT and the
1007 engineered *TgPRP4K* mutant strains (F647S, L686F, L715F). The EC₅₀ values on the upper
1008 part of the graphs represent the mean \pm SD of three biological replicates. On the top of each
1009 panel, lines shown the fold change in EC₅₀ relative to that of the WT parasites. Dose-response
1010 curves are shown in [Extended Data Fig. 3c](#). **g**, Effects of *TgPRP4K* mutations on *T. gondii* lytic
1011 cycle as determined by plaque assay. Plaque sizes (n = 50 per condition) were measured for
1012 WT and the engineered *TgPRP4K* mutant strains (F647S, L686F, L715F) after 7 days of growth
1013 in the absence or presence of 300 mM of altiratinib. n.d., not detected. Significance was
1014 assessed by Mann-Whitney or Kruskal-Wallis tests (One-way ANOVA).

1015
1016 **Fig. 3 | Structure of the complex *TgPRP4K*-altiratinib and mechanism of action. a,**
1017 Thermal stability profile of WT (upper panel) and L715F (bottom panel) recombinant proteins.
1018 Each protein was incubated for 3 minutes at different temperatures (from 30° to 69° C) in
1019 presence or absence of Altiratinib (100 μ M) to quantify the melting temperatures using non-
1020 linear regression analysis of normalized data and assuming a sigmoidal dose response. **b,**
1021 Protein–Ligand interaction. WT and L715F recombinant proteins labelled to His-fluorescent
1022 dye (200nM), were incubated with altiratinib from 105 nM to 6.1 nM. Changes in

1023 thermophoresis were plotted, yielding a K_d of 4808 ± 1816 nM for WT (upper panel) and 503.8
1024 ± 70 nM for L715F (bottom panel). Error bars: dotted lines; $n= 3$. **c**, Full structure of *TgPRP4K*
1025 (L715F) bound to altiratinib (pdb id: [7Q4A](#)). PRP4K is represented in a cartoon fashion with a
1026 transparent surface background with alpha helices colored in orange and beta strands colored
1027 in yellow. The activation loop is highlighted in blue, the DFG backbone is shown in pink, the
1028 phosphor-serine 729 side chain and altiratinib are shown in a stick representation and colored
1029 in grey and cyan respectively. **d**, Altiratinib binding within *TgPRP4K*. Zoomed in focus on
1030 altiratinib and the key interacting side chains of *TgPRP4K* shown as grey sticks. Cartoon colors
1031 are the same as used in panel a. **e**, Sequence alignment of altiratinib *TgPRP4K* binding regions
1032 compared against *Plasmodium falciparum* (*Pf*), *Chromera Velia* (*cc*), *Schizosaccharomyces*
1033 *pombe* (*Sp*), *Arabidopsis thaliana* (*At*) and *Homo sapiens* (*Hs*) PRP4K/CLK3 orthologs. Key
1034 regions are highlighted by pink rectangles, altiratinib interacting amino acids from *TgPRP4K*
1035 are shown by cyan circles while divergent residues in the human ortholog are shown by red
1036 triangles. Mutations found in the mutagenesis experiment are highlighted by a green star.

1037
1038 **Fig. 4 | Hinge region selectivity towards altiratinib.** **a**, Hinge region species selectivity
1039 towards altiratinib. Cartoon diagram of structurally superposed *TgPRP4K* (tan) and human
1040 PRPF4B (sky blue) with altiratinib in cyan. Hinge region residues are detailed by including
1041 stick representations of their side chains. **b**, Sanger chromatogram validating the *TgPRP4K*
1042 gene editing for W649P mutation. On the top, nucleotide positions relative to the ATG start
1043 codon on genomic DNA are indicated. **c**, IFA showing the W649P resistance to altiratinib.
1044 Confluent HFFs were infected with engineered parasites and incubated with pyrimethamine (1
1045 μ M) or altiratinib (300 nM) for 24h. Fixed cells were stained using anti-GAP45 antibody
1046 (magenta) while the cytosolic GFP is showed in green. Scale bar represents 5 μ m. **d**, Graph
1047 representing the EC_{50} of W649P for pyrimethamine and altiratinib. Values showed in the upper
1048 part on the graph are the mean \pm SD of three independent experiment. On the top of the panel,
1049 the line shows the fold change in altiratinib EC_{50} relative to pyrimethamine. **e**, Plaque assay
1050 representing the lytic cycle of RH WT and W649P parasites in presence or absence of
1051 altiratinib. After 7days of drugs incubation, infected cells were fixed and stained to visualize
1052 the presence of lysis plaques (on the left). The area of 50 plaques was measured and represented
1053 in the right panel. **f**, Thermal stability profile of W649P recombinant protein in presence or
1054 absence of Altiratinib. **g**, Protein-ligand interaction profile of W649P protein in presence of
1055 Altiratinib. Changes in thermophoresis of three replicates were plotted. Error bars: dotted lines.

1056 NA, not available. **h**, Table showing the melting temperature (T_m) of WT, L715F and W649P
1057 recombinant proteins during their incubation with DMSO or Altiratinib at different
1058 temperatures. Low interaction between W649P and the compound was detected as showed by
1059 the ΔT_m values.

1060

1061 **Fig. 5 | Nanopore DRS analysis of altiratinib-induced splicing defects in *T. gondii*.** **a**,
1062 General transcriptomic effects of altiratinib treatment. *k*-means clustering of 2400 transcripts
1063 treated with EdgeR: $\log_2(\text{CPM}+4)$. The color key ranges from -3 to 3 (green to red), 3 clusters
1064 were defined. In each, *TgPRP4K* WT/L715F/W649P duplicate sequencing experiments are
1065 shown in the presence or absence of altiratinib. **b**, M-pileup representation of the aligned
1066 nanopore reads at the *TGME49_214940* loci. WT/L715F/W649P sequencing experiments are
1067 shown as grayscale histograms in the presence or absence of altiratinib. **c and d**, FLAIR
1068 analysis of *TGME49_211420* (**c**) and *TGME49_214940* (**d**) loci. Standard annotation and
1069 FLAIR collapsed isoforms (FCI) are shown schematically under a sample view of 15 reads per
1070 condition (same conditions as in **b**). Sense and antisense reads are colored red and blue,
1071 respectively. Below the FCI representation is an isoform quantification histogram showing
1072 duplicate measurements in each WT/L715F/W649P and untreated (-) or treated (+) condition.
1073 The color code is the same as for the above FCI, grey histograms represent minor isoforms
1074 which not shown schematically. **d**. Overall quantification of intron retention. Scatter plot of
1075 intron retention ratios (per averaged duplicate transcript) are shown for *T. gondii* and *H.*
1076 *sapiens*. WT/L715F/W649P strains that were untreated (in green) or treated (in cyan) are
1077 shown, the black histogram shows the median, the whiskers show the interquartile range.
1078 Significance between the WT untreated and treated conditions was calculated using a non-
1079 parametric Friedman test.

1080

1081 **Fig. 6 | Cross-species selectivity of altiratinib analysed by nanopore DRS.** **a**, Splicing
1082 defects induced by altiratinib in *P. falciparum*. M-pileup representation of aligned nanopore
1083 reads at the *PF3D7_0918100* and *PF3D7_1118700* loci. Untreated (UT) or altiratinib-treated
1084 sequencing experiments are shown as grayscale histograms. Shown below are IGB samples
1085 from 10 individual aligned reads using sense (purple) and antisense (blue) coloring under UT
1086 and treated conditions. **b**, Overall quantification of intron retention in *P. falciparum*. Scatter
1087 plots of intron retention ratios (per averaged duplicate transcript) are shown for untreated (in
1088 green) or treated (in cyan) conditions, the black histogram shows the median, the whiskers show
1089 the interquartile range. Significance between the WT untreated and treated conditions was

1090 calculated using a nonparametric Mann-Whitney *t*-test. **c**, Splicing consistency is maintained in
1091 *C. parvum*. M-pileup and IGB sampling of aligned reads from untreated (UT) or treated *C.*
1092 *parvum* at the highly transcribed and spliced *cdg6_4620* loci. **d**, Overall quantification of intron
1093 retention in *C. parvum*. The same display rules as in **b**. were applied. **e**. Hinge region species
1094 selectivity towards TCDM-135051. Cartoon diagram of the structurally superposed *TgPRP4K*
1095 from this work (in tan) and the alphaflod2 predicted *PfCLK3* (dodger blue) with TCDM-135051
1096 modelling in orange. The residues of the hinge region are also detailed by showing their side
1097 chains as stick representations. **f**, Thermal shift assay of *TgPRP4K* and *PfCLK3* in the presence
1098 of altiratinib or TCDM-135051.

1099

1100 **Extended Data Fig. 1 | Identification of altiratinib by a medium-throughput screening of**

1101 **an FDA-approved library. a**, Schematic overview of the workflow used to screen the library

1102 of 514-FDA approved compounds. Confluent HFFs were infected for 2 hours with tachyzoites

1103 of the *T. gondii* RH strain expressing the NanoLuc luciferase (RH $\Delta ku80$ *UPRT::NLuc-P2A-*

1104 *EmGFP*). Each compound was then added to the culture at a concentration of 5 μ M for 48h.

1105 After washing and incubation with furimazine substrate, luciferase activity was detected to

1106 select hits. Hits were further validated by testing their efficiency at 1 μ M and checking stability

1107 over time or toxicity to the host cells. **b**, Distribution of 84 hits by pathway inhibition. **c**,

1108 Mitochondrial toxicity assay. Human cells were incubated with increasing concentrations of

1109 altiratinib, sodium azide (positive control for mitochondrial toxicity) or 800 μ g/ml of digitonin

1110 (positive control for cell toxicity). After 90 min, cell viability (cytotoxicity) was detected by

1111 fluorescence readout, while ATP production was measured by luminescence as indicated in the

1112 “*Mitochondrial ToxGloTM Assay*” kit (Promega). Plots are representative of two biological

1113 replicates. **d**, Representation of *T. gondii* cytotoxicity after incubation with drugs. Confluent

1114 HFFs were infected with the strain RH WT (RH $\Delta ku80$ *UPRT::NLuc-P2A-EmGFP*) and

1115 incubated with 1 μ M of pyrimethamine or 300nM of altiratinib for 16h. After 3 and 6 days, the

1116 drugs were washed out and the cells were stained with Coomassie blue to detect the presence

1117 of plaques. Graphs show the size of visible plaques in each condition. n.d., not detected.

1118 Statistical analyses were performed using Mann-Whitney test (One-way ANOVA). **e**,

1119 Workflow used to map mutations that confer resistance to altiratinib in parasites.

1120

1121 **Extended Data Fig. 2 | Origin and interactome of TgPRP4K. a**, Phylogenetic analysis of

1122 CLK-, PRP4K- and SRKP-like families. The unrooted phylogenetic tree was inferred from the

1123 kinase domain alignment. The tree was computed with the neighbor-joining algorithm, based
1124 on an HMM multiple alignment. The bootstrap values are shown in blue. The reliability of
1125 branching was assessed by the bootstrap resampling method using 1000 bootstrap replicates. **b**
1126 **and c**, Size-exclusion chromatography of PRP4K- and PRP8-containing complexes after Flag-
1127 affinity selection. The fractions were analysed using western blots to detect PRP4K- or PRP8-
1128 HAFlag (anti-HA antibodies) (**b**) and on silver-stained SDS-PAGE gels (**c**).

1129

1130 **Extended Data Fig. 3 | Identification and validation of the molecular target *TgPRP4K*. a,**
1131 Strategy for introducing point mutations into *T. gondii* parasites. Focus on the *TgPRP4K* locus
1132 and CRISPR/Cas9-mediated homology-directed repair with single-stranded oligo DNA
1133 nucleotides (ssODNs) carrying nucleotide substitutions (red letters). After homologous
1134 recombination (HR) events, the *TgPRP4K* recombinant parasites were selected with altiratinib.
1135 The engineered parasites were then validated by Sanger sequencing. **b**, Sanger chromatograms
1136 validating *TgPRP4K* gene editing. Indicated are the nucleotide positions relative to the ATG
1137 start codon on the genomic DNA. **c**, Dose-response curves for inhibition of *T. gondii* growth
1138 in response to increasing concentration of the indicated compounds. Confluent HFF monolayer
1139 were infected with WT and the engineered *TgPRP4K* mutant strains expressing the NanoLuc
1140 luciferase. Data are presented as mean \pm standard deviation (SD) of n=3 technical replicates
1141 from a representative experiment out of at least two independent biological assays. Shaded error
1142 envelopes depict 95% confidence intervals.

1143

1144 **Extended Data Fig. 4 | Insect-cell recombinant expression of *TgPRP4K*. a,** PRP4K full
1145 protein organization. IUpred disorder propensity prediction is shown above a linear schematic
1146 representation of the polypeptide chain. Phosphorylated and Acetylated residues (data extracted
1147 from ToxoDB.org) are highlighted in blue and red respectively. **b**, SEC-MALLS measurement
1148 of *TgPRP4K* sample homogeneity. UV(280nm) absorbance chromatogram of insect cell
1149 purified WT (in blue) or L715F mutant (in green) *TgPRP4K* (534-895) combined to a mass
1150 calculation as a scatter plot with the Y axis (in KDa) on the right when run on a S200 increase
1151 column. **c**, SDS PAGE gel of recombinantly produced PRP4K. WT (left) and L715F (right)
1152 purified protein analysed a NuPage 5-12% Bis-Tris gel run in MES buffer and colored with
1153 Coomassie blue. The indicated numbers correspond to protein marker mass in kDa.

1154

1155 **Extended Data Fig. 5 | Crystal structure specificities of *TgPRP4K*. a,** Crystallographic
1156 dimerization of *TgPRP4K*. Cartoon representation of chain/monomer A and B colored green

1157 and orange respectively. Altiratinib is displayed as sticks in cyan. **b**, Phosphotyrosine 729
1158 mediated crystal contacts. Cartoon and stick representation of the phosphotyrosine and
1159 interaction side chains from homo-monomeric and symmetry related molecules. 2mFo-DFc
1160 electron density is represented at an rmsd of 1.72. This specific representation was done using
1161 pymol. **c**, Structural conservation of *TgPRP4K* compared to the human *HsPRPF4B*. Structural
1162 alignment shown in a cartoon fashion between *TgPRP4K* bound to altiratinib (tan), ADP bound
1163 *HsPRPF4B* (skye blue) and *HsPRPF4B* (magenta) bound to cmp 224. Certain regions are
1164 shown enlarged for more detail.

1165

1166 **Extended Data Fig. 6 | Altiratinib binding site and interaction network.** **a**, Altiratinib omit
1167 map. Altiratinib mFo-DFc omit map (generated in coot) at 4.2 rmsd showing electron density
1168 as a green/grey mesh and the altiratinib stick structure in green. **b**, ATP and allosteric pocket
1169 binding of altiratinib. Cartoon representation combined with a surface and hydrophobic
1170 attribute coloring (in yellow). Notable side chains involved in hydrophobic interactions are
1171 displayed as stick side chains. **c**, Ligplot schematic 2D representation of all residues interacting
1172 with altiratinib. Charged interactions are displayed as green dotted lines whereas hydrophobic
1173 interactions are shown with red curved-in combs.

1174

1175 **Extended Data Fig. 7 | DRS examples of altiratinib induced splicing defects in *Toxoplasma***
1176 ***gondii*.** FLAIR analysis of *TGME49_247350* (**a**), *TGME49_208450* (**b**) and *TGME49_278940*
1177 (**c**) loci. Standard annotation and FLAIR collapsed isoforms (FCI) are shown schematically for
1178 all panels under a sample view of 15 reads per condition. Sense and antisense reads are colored
1179 red and blue, respectively. Below the FCI representation is an isoform quantification histogram
1180 showing duplicate measurements in each WT/L715F/W649P and untreated (-) or treated (+)
1181 condition. The color code is the same as for the above FCI, grey histograms represent minor
1182 isoforms that are not schematically represented.

1183

1184 **Extended Data Fig. 8 | DRS examples of altiratinib treatment on *Plasmodium falciparum***
1185 **and *Cryptosporidium parvum*.** FLAIR analysis of *PF3D7_0414900* (**a**), *PF3D7_0528400* (**b**),
1186 *PF3D7_1319400* (**c**) and *PF3D7_* loci in *Plasmodium falciparum* as well as the *cgd6_3190*
1187 loci (**d**) in *Cryptosporidium parvum*. Standard annotation and FLAIR collapsed isoforms (FCI)
1188 are shown schematically for all panels under a sample view of 15 reads per condition. Sense
1189 and antisense reads are colored purple and blue, respectively. Below the FCI representation is
1190 an isoform quantification histogram showing duplicate measurements in untreated (-) or treated

1191 (+) condition. The color code is the same as for the above FCI, grey histograms represent minor
1192 isoforms that are not schematically represented. **e**, Sequence alignment of the *TgPRP4K*
1193 binding regions of altiratinib compared to PRP4K/CLK3 orthologs of *Plasmodium falciparum*
1194 (*Pf*), *Cryptosporidium parvum* (*Cp*) and *Homo sapiens* (*Hs*). Key regions are highlighted by
1195 pink rectangles, altiratinib interacting amino acids from *TgPRP4K* are shown by cyan circles,
1196 while divergent residues at the same position in the orthologs of *Cp* and *Hs* are shown in red.

1197

1198 **Extended Data Fig. 9 | Biochemistry of recombinant *PfPRP4K*.** SEC-MALLS
1199 chromatogram of homogeneity of *PfPRP4K* sample. UV (280 nm) absorbance chromatogram
1200 of insect cell-purified *PfPRP4K* (aa 336-692 with the C339 mutated to a S) combined to a mass
1201 calculation as a scatter plot with the Y axis (in KDa) on the right when run on a S200 increase
1202 column. Next to the chromatogram is a NuPAGE 4-12% gel of the same purified sample run in
1203 MES and stained with Coomassie blue. The numbers shown correspond to the marker mass in
1204 kDa.

1205

1206

1207 **Supplementary files**

1208 **Supplementary Fig. 1 | Domain architectures of proteins purified together with PRP4K**
1209 **and PRP8.** Representative domain architectures of *T. gondii* PRP4K and PRP8 partners
1210 identified by mass spectrometry-based proteomics ([Supplementary Table 3](#)) are shown.
1211 Domains were predicted by SMART and PFAM.

1212

1213 **Supplementary Table 1 | Table describing the 514 compounds in the TargetMol© FDA-**
1214 **approved compound library.**

1215

1216 **Supplementary Table 2 | Mutations found in candidate genes by RNA-sequencing analysis**
1217 **of altiratinib-resistant mutants.** Amino acid substitutions with corresponding codons shown
1218 in parentheses are indicated for each *T. gondii*-resistant mutant strain.

1219

1220 **Supplementary Table 3 | Mass spectrometry-based characterization of the interactomes**
1221 **of PRP4K and PRP8.** *TgPRP4K*- and *TgPRP8*-containing complexes were purified by affinity
1222 using FLAG tagging and subjected to size exclusion chromatography. Proteins present in the
1223 different eluted fractions were pooled and separated by SDS-PAGE. For *TgPRP4K*, two lanes

1224 were analyzed with pools of fractions 24 and 26, and fractions 28 and 30. For *TgPRP8*, three
1225 lanes were analyzed with fractions 14, 16 and 18, fractions 20 and 22, and fractions 24 and 26
1226 (see below). The bands of interest in each lane, marked with arrows below, were excised and
1227 analyzed using MS-based proteomics. The parasite proteins identified and quantified in each
1228 band of the *TgPRP4K*- and *TgPRP8*-containing complexes are listed in the following tables.

1229

1230 **Supplementary Table 4 | Statistics of crystallographic data.**

1231

1232 **Supplementary Table 5 | Description of *T. gondii* strains, plasmids and primers.** List of *T.*
1233 *gondii* parasite lineages as well as plasmids used in this work. Primers used in this work are
1234 also listed.

1235

1236 **Supplementary Data File 1 | Full PDB X-ray structure validation report** of crystal structure
1237 of *Toxoplasma* *TgPRP4K* with altiratinib (pdb id: [7Q4A](#)).

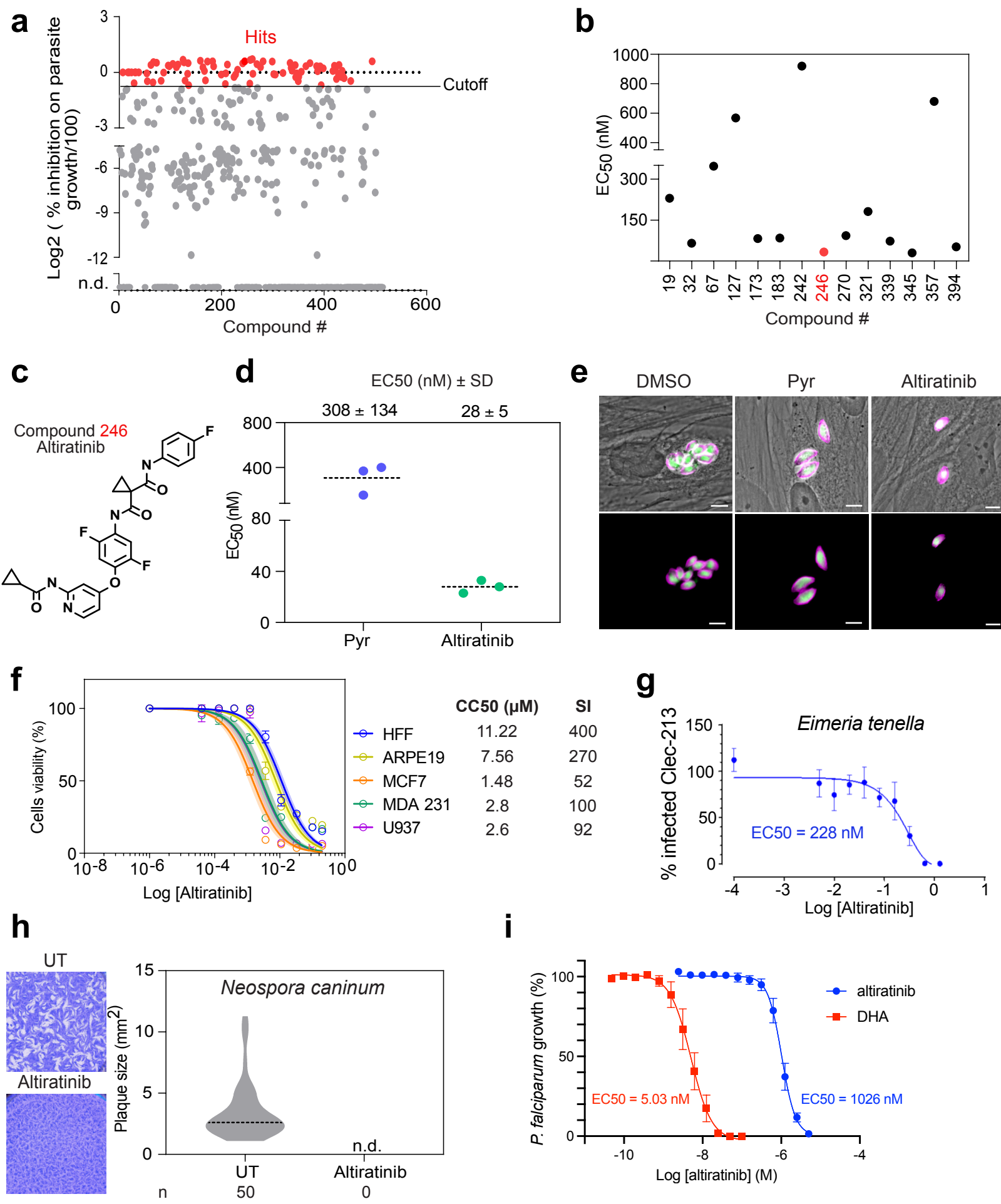


Figure 1

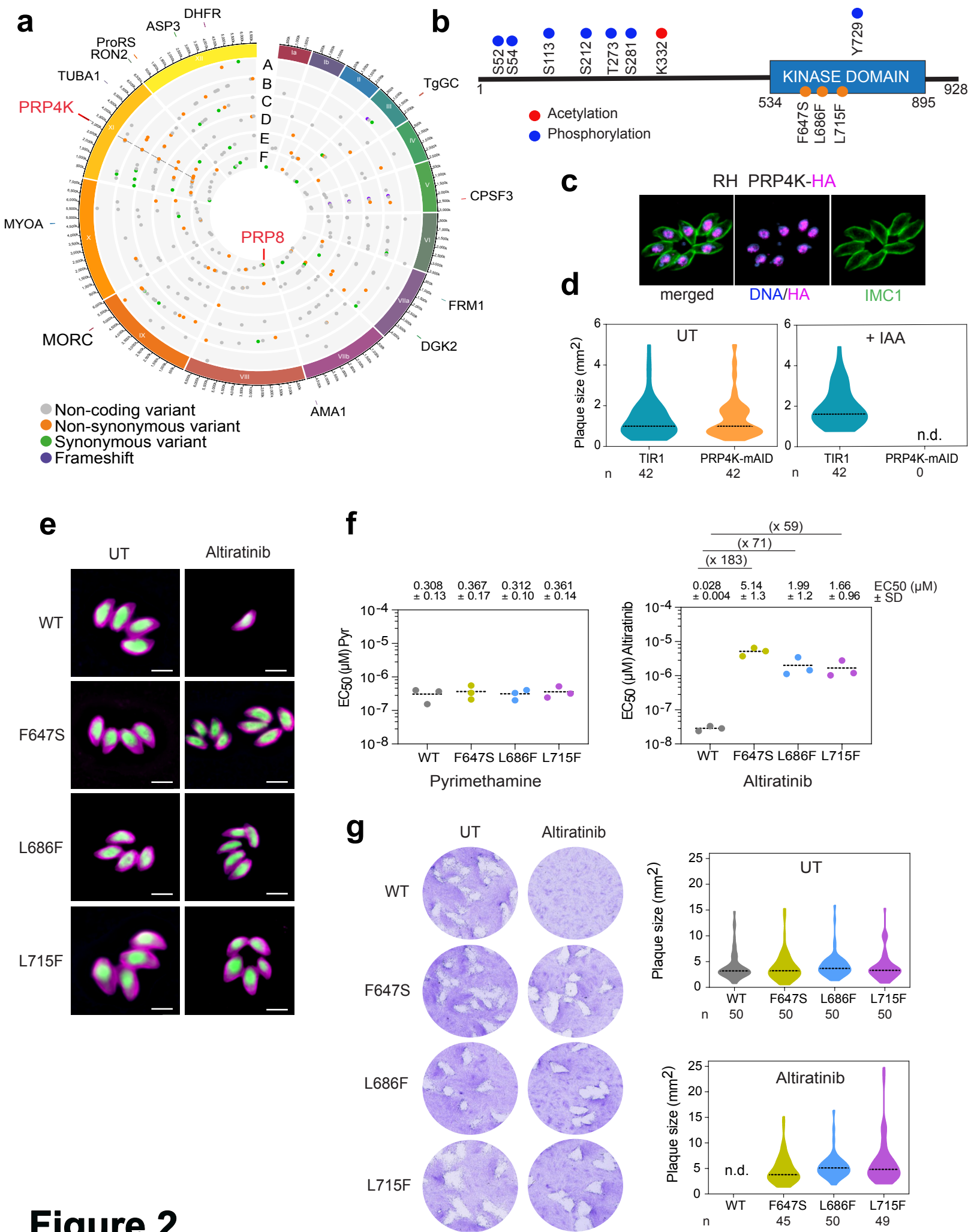
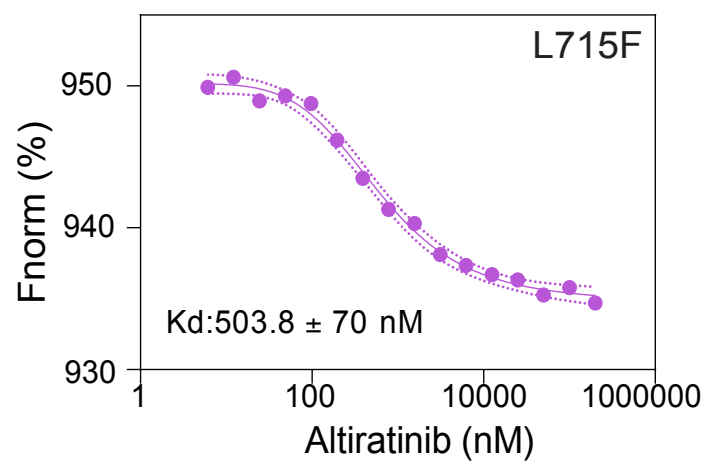
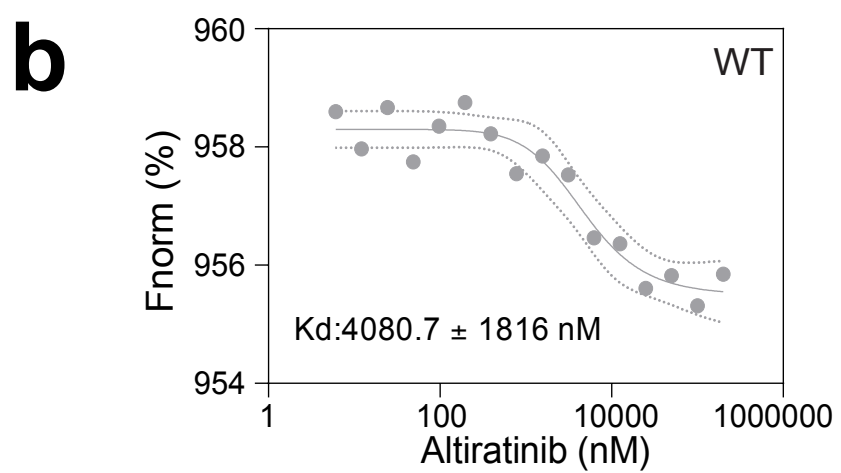
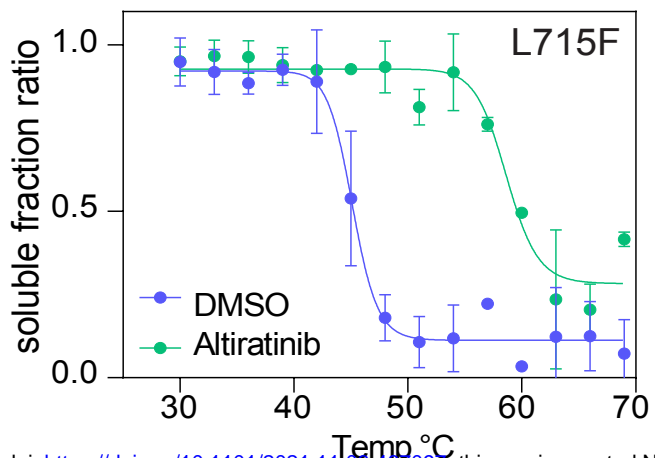
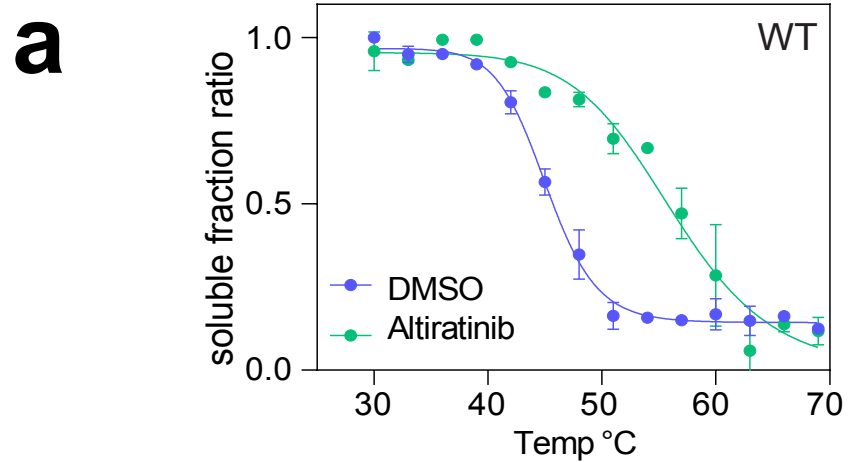
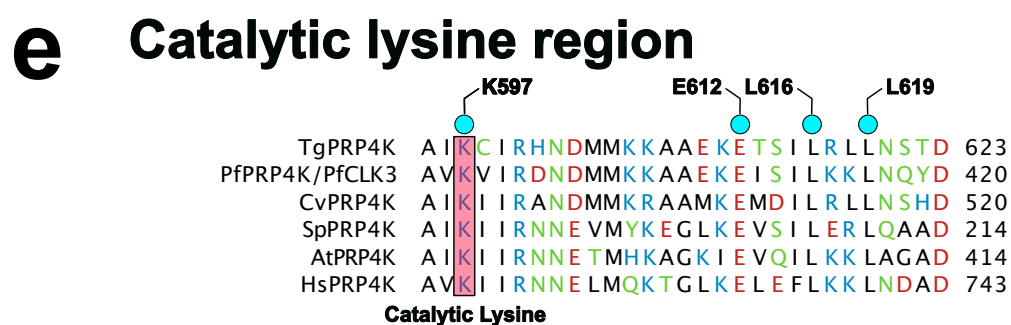
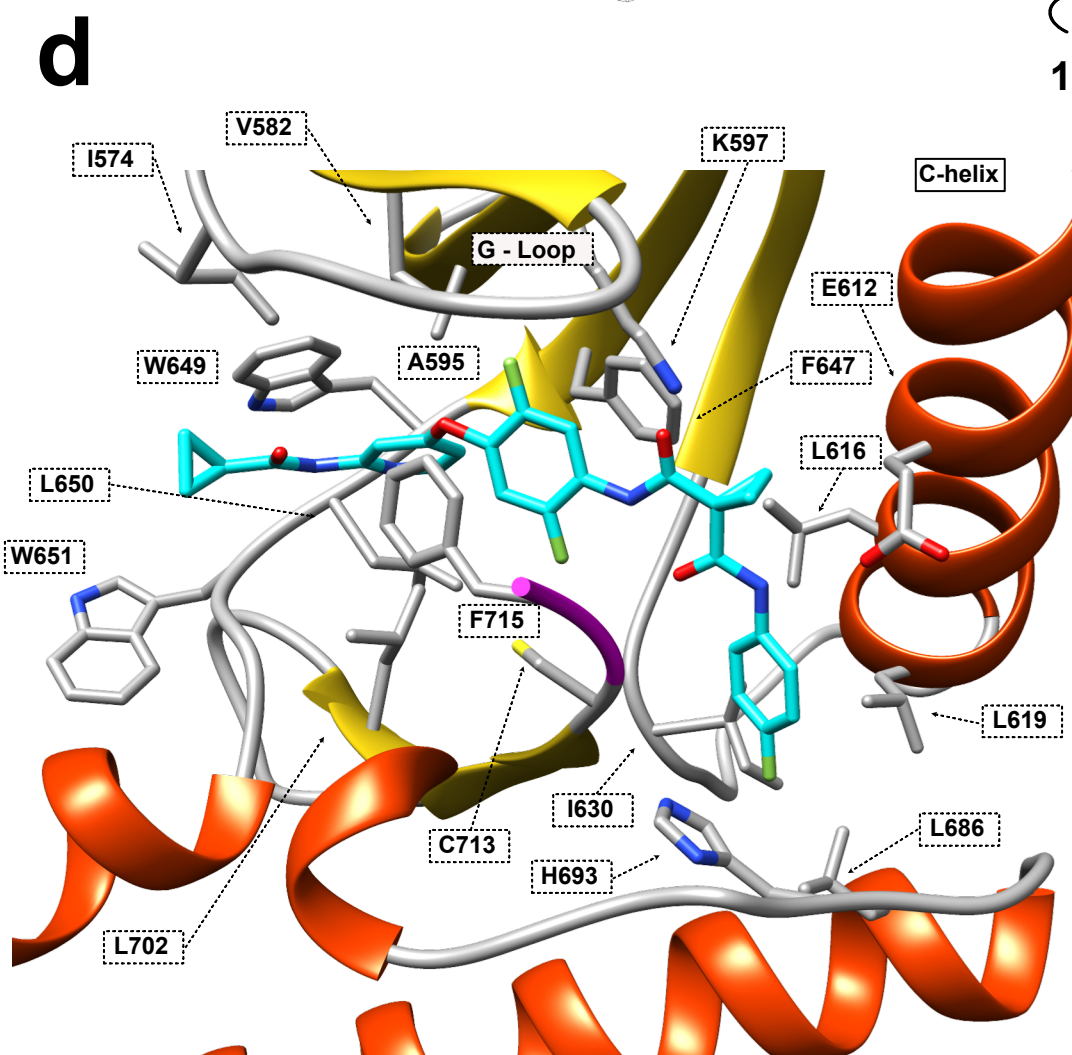
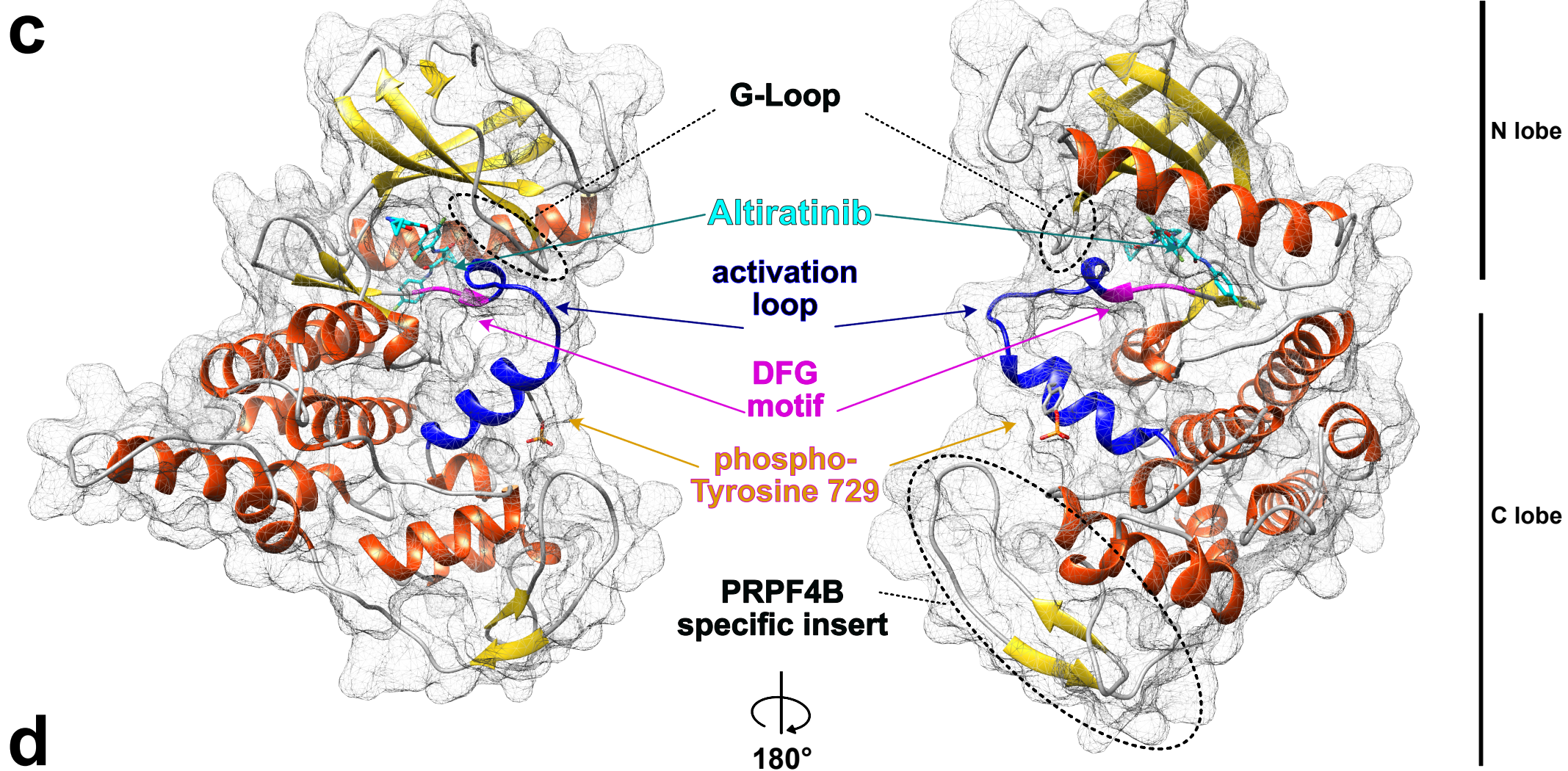


Figure 2



bioRxiv preprint doi: <https://doi.org/10.1101/2021.11.03.467097>; this version posted November 3, 2021. The copyright holder for this preprint (which was not certified by peer review) is the author/funder. All rights reserved. No reuse allowed without permission.



Adenosine specificity pocket



DFG motif

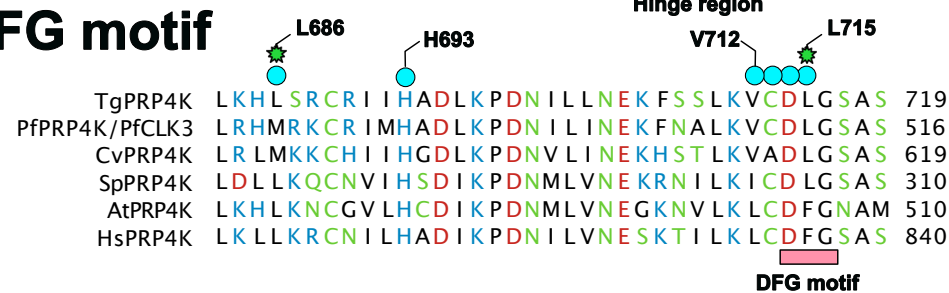


Figure 3

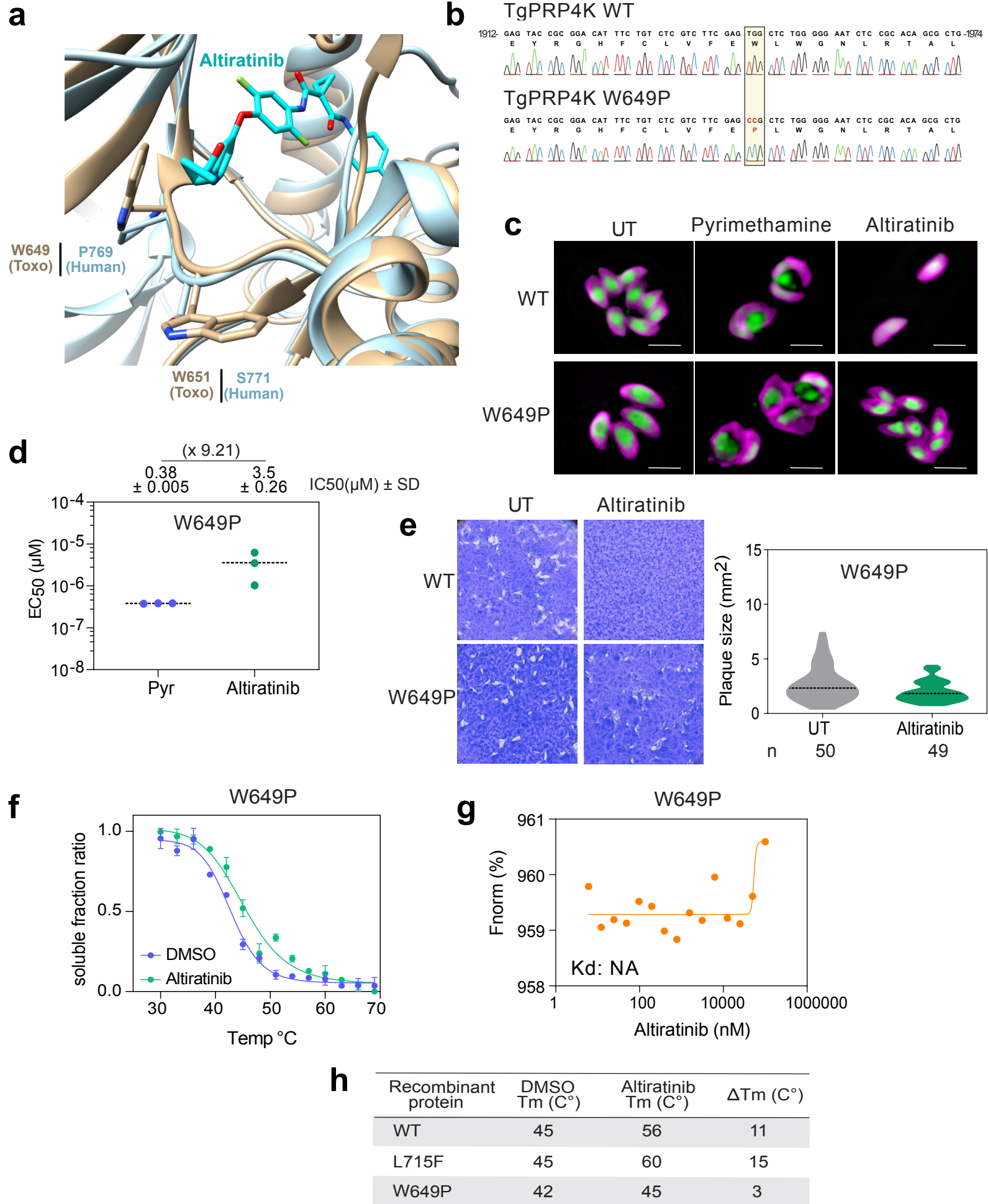


Figure 4

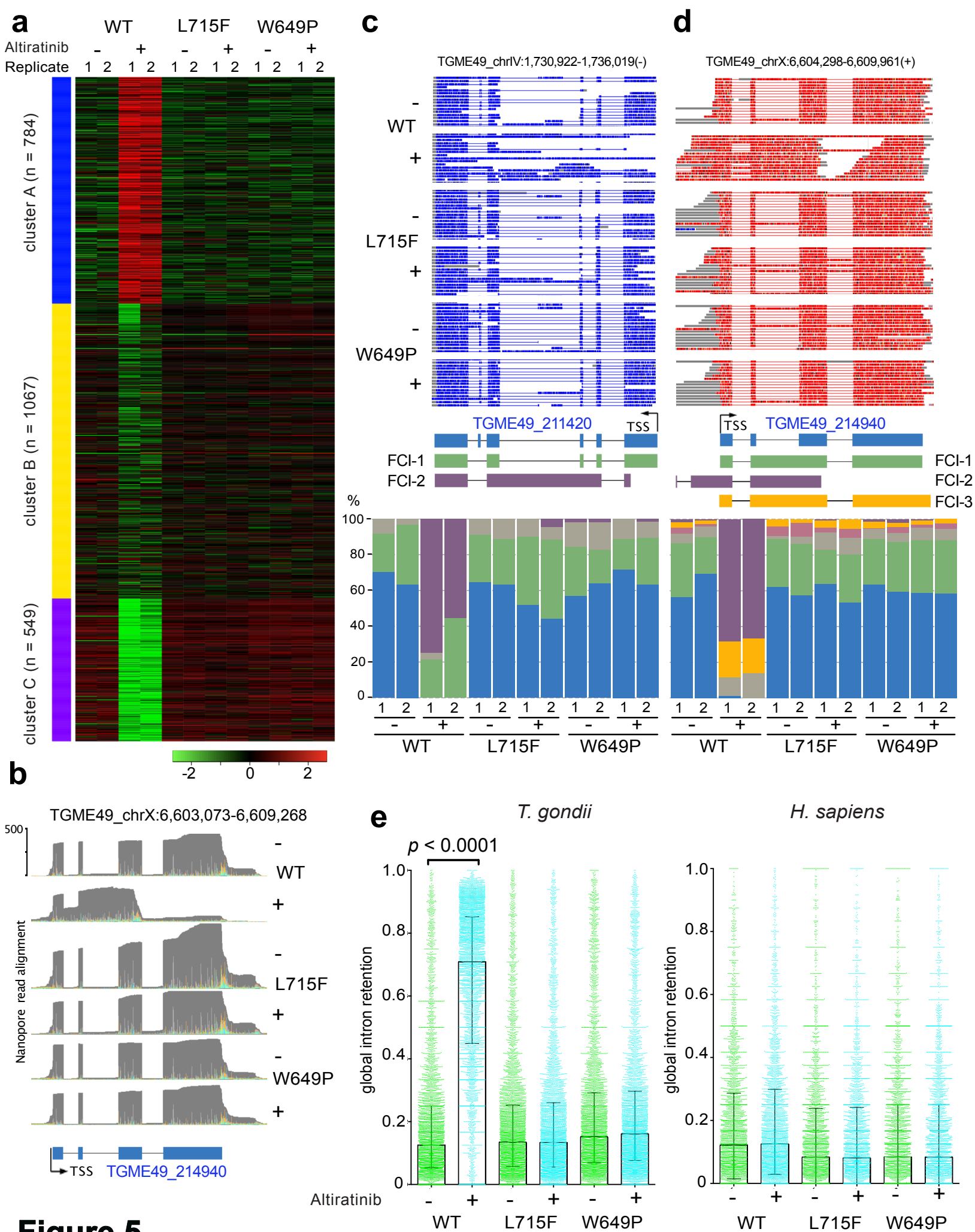


Figure 5

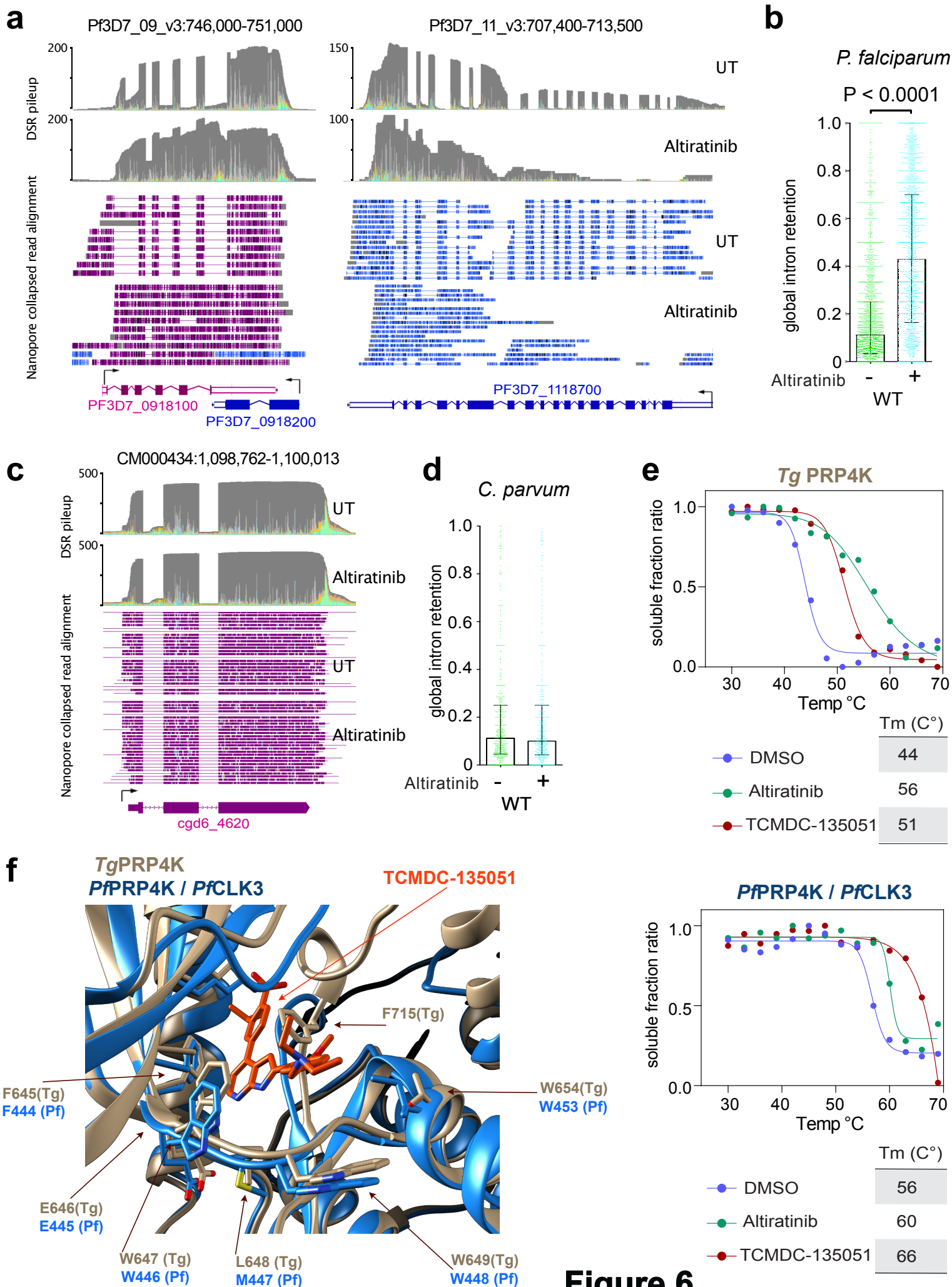
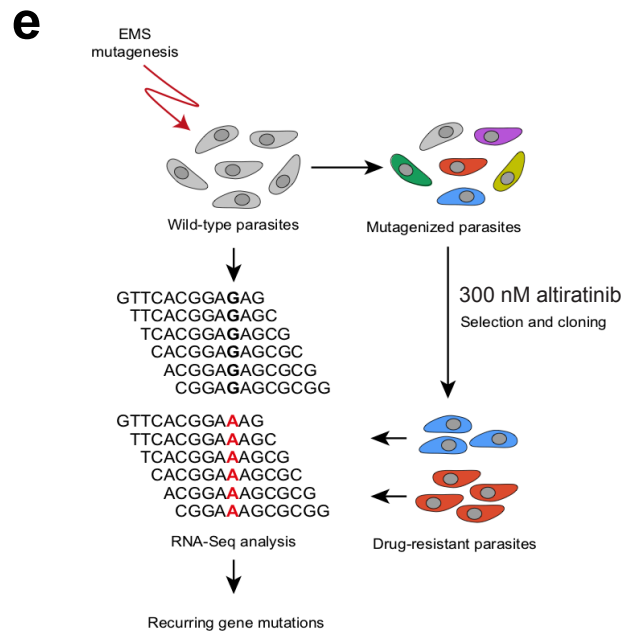
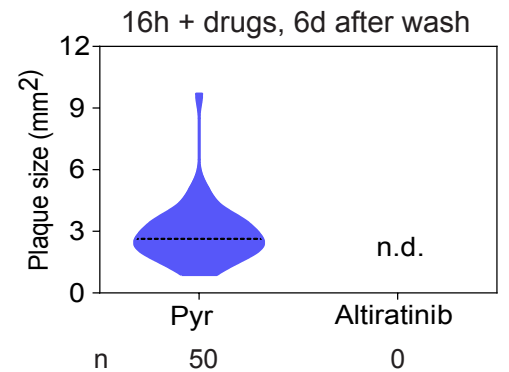
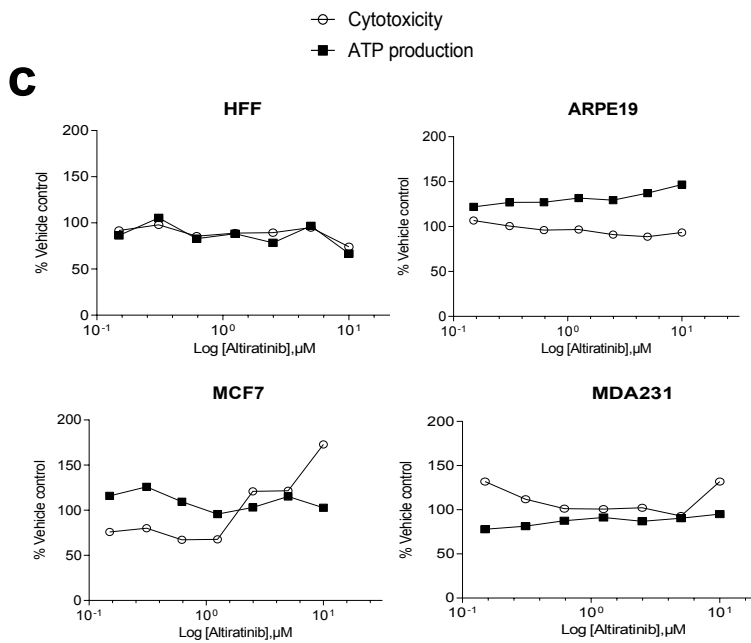
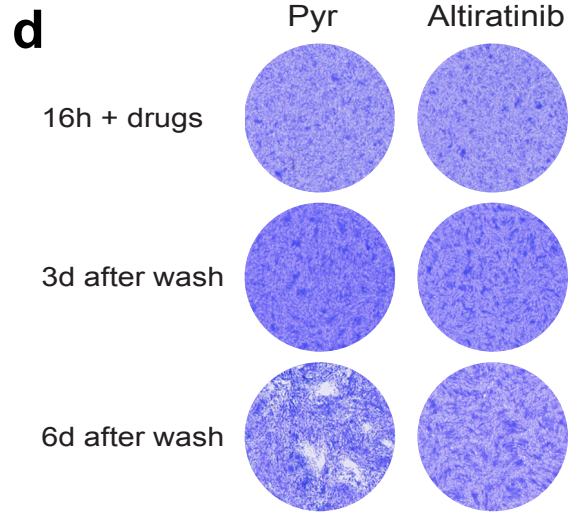
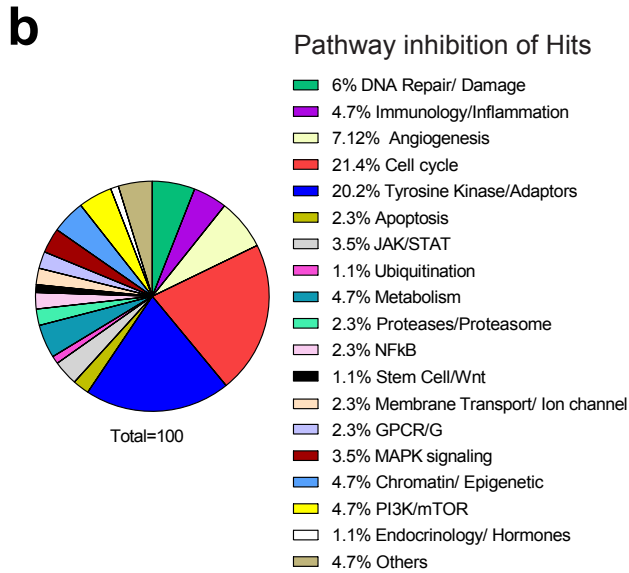
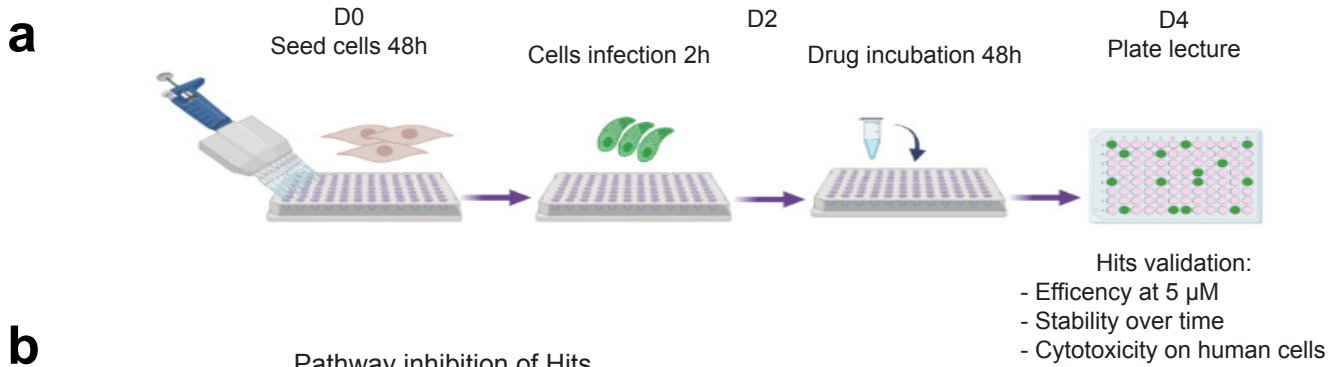


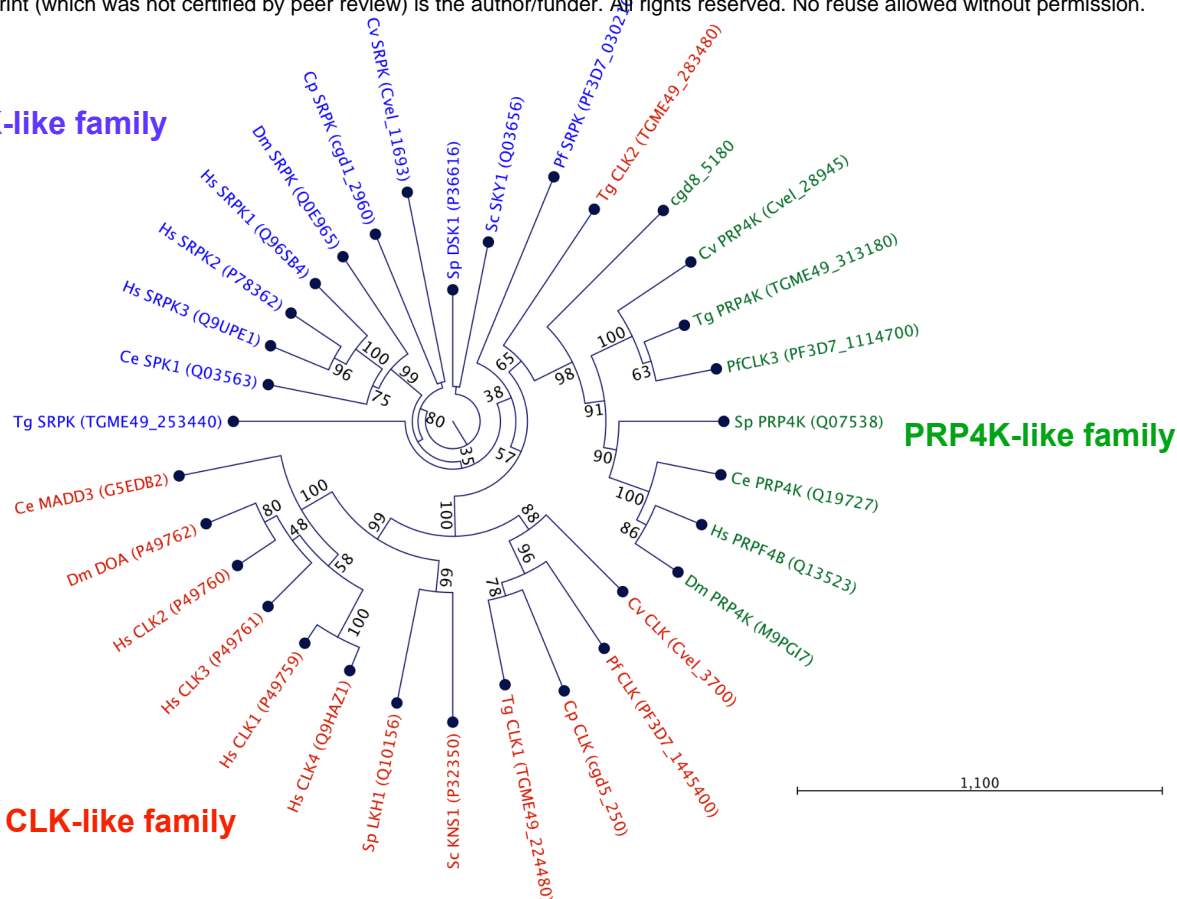
Figure 6



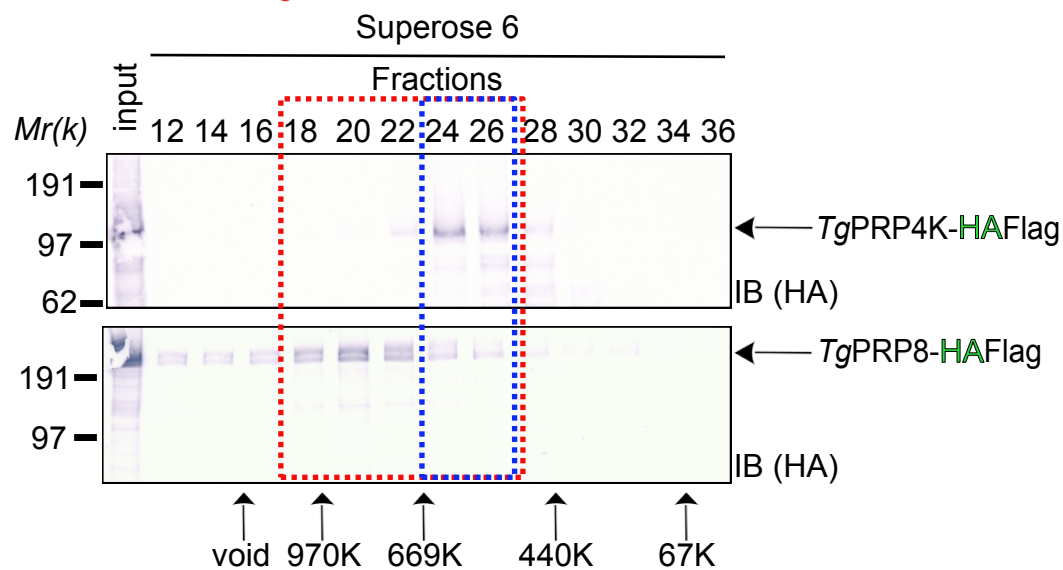
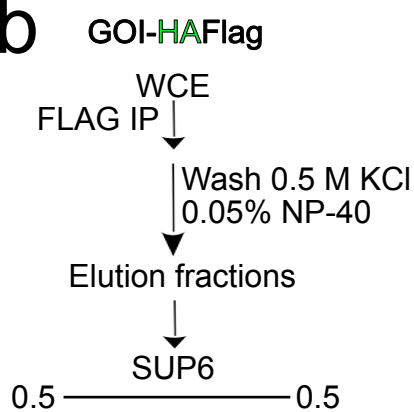
Extended Data Fig. 1

a

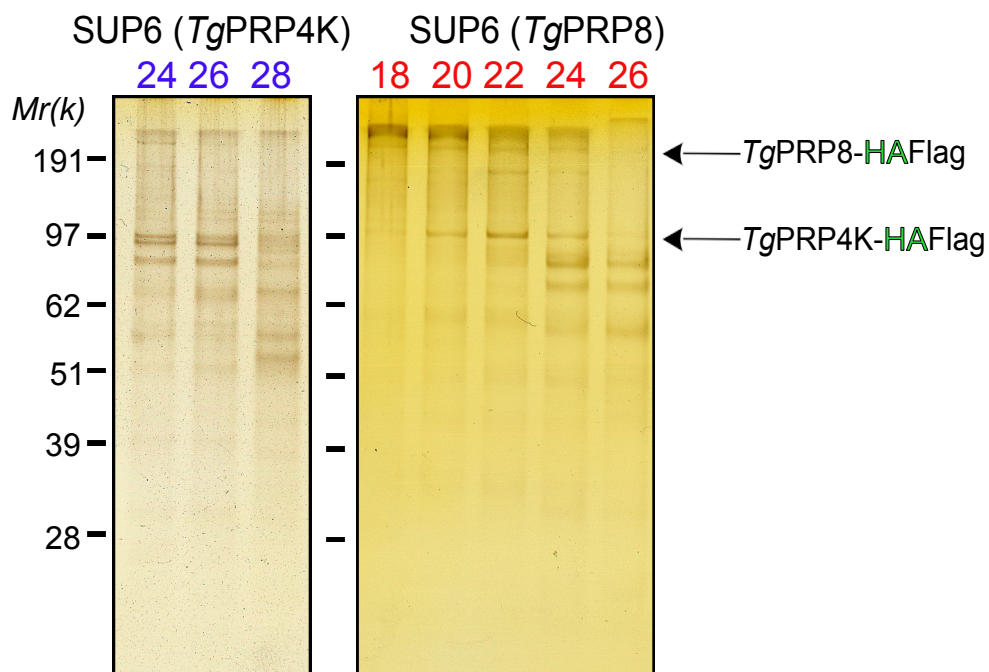
SRPK-like family

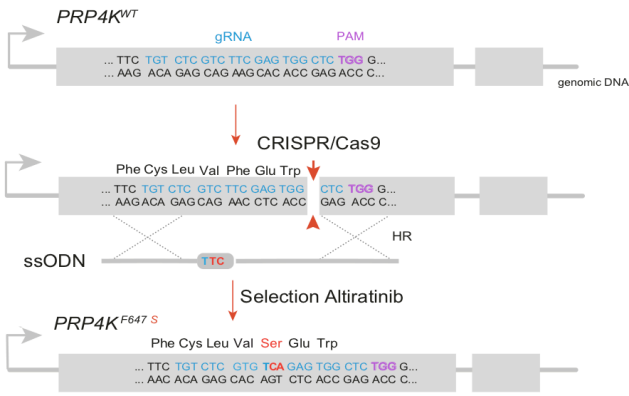
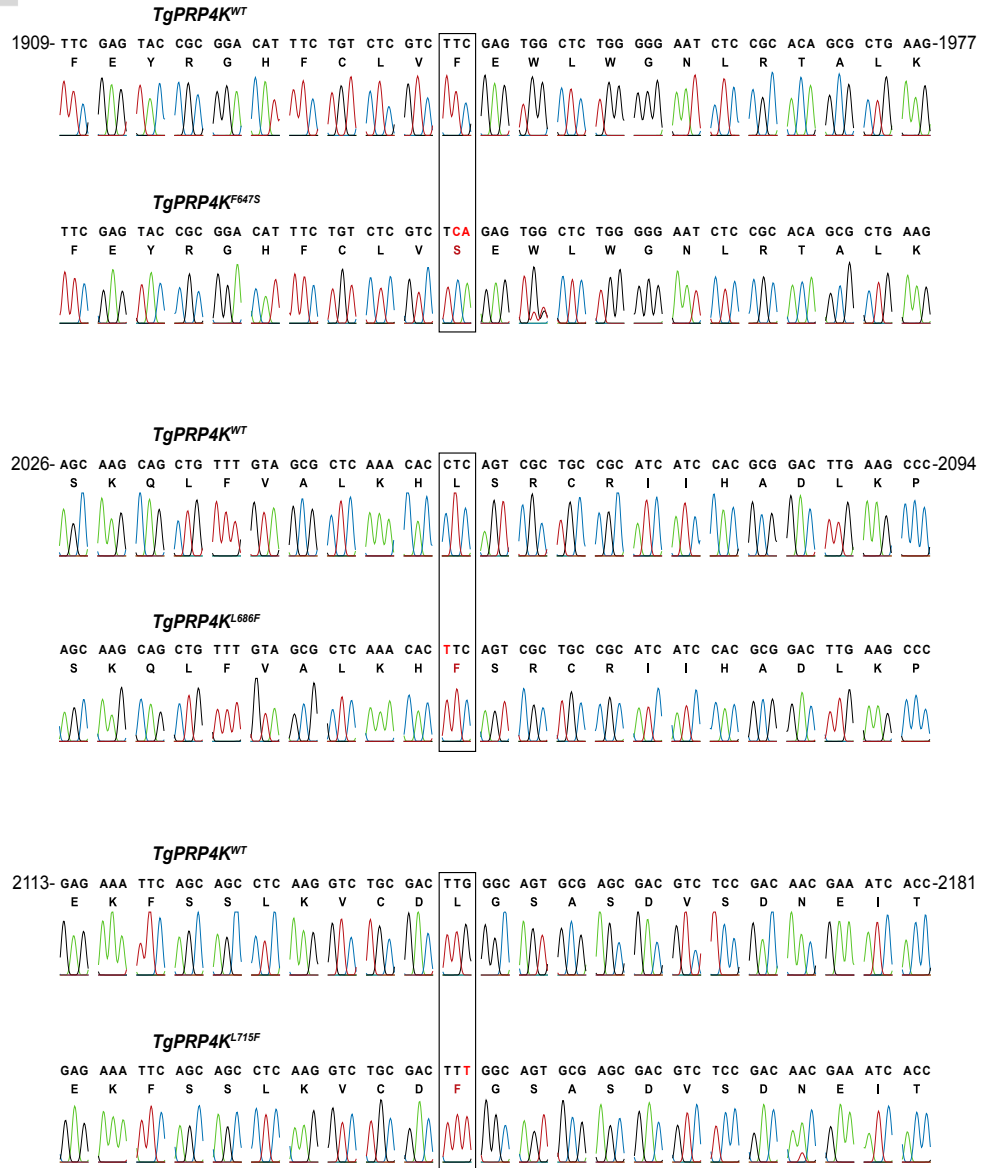
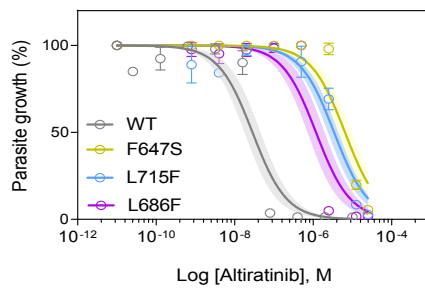
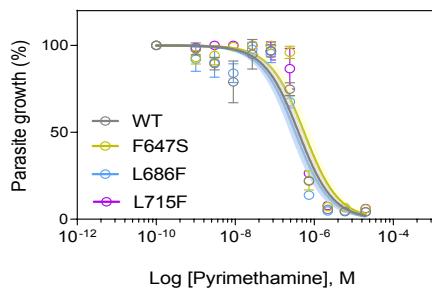


b

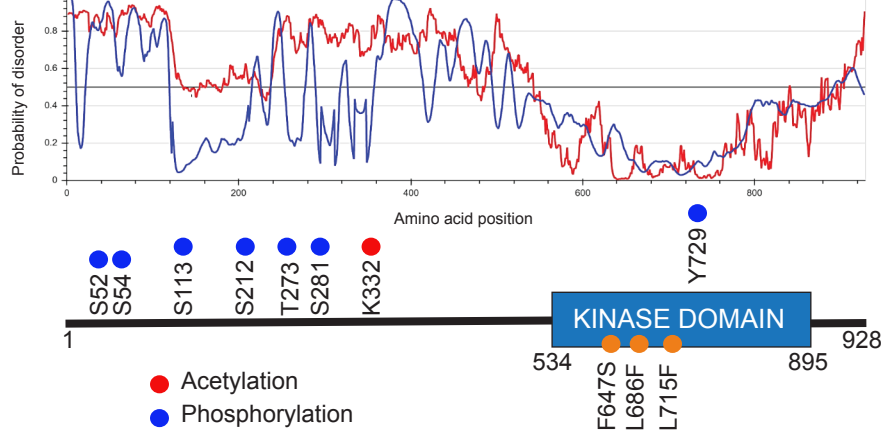


c

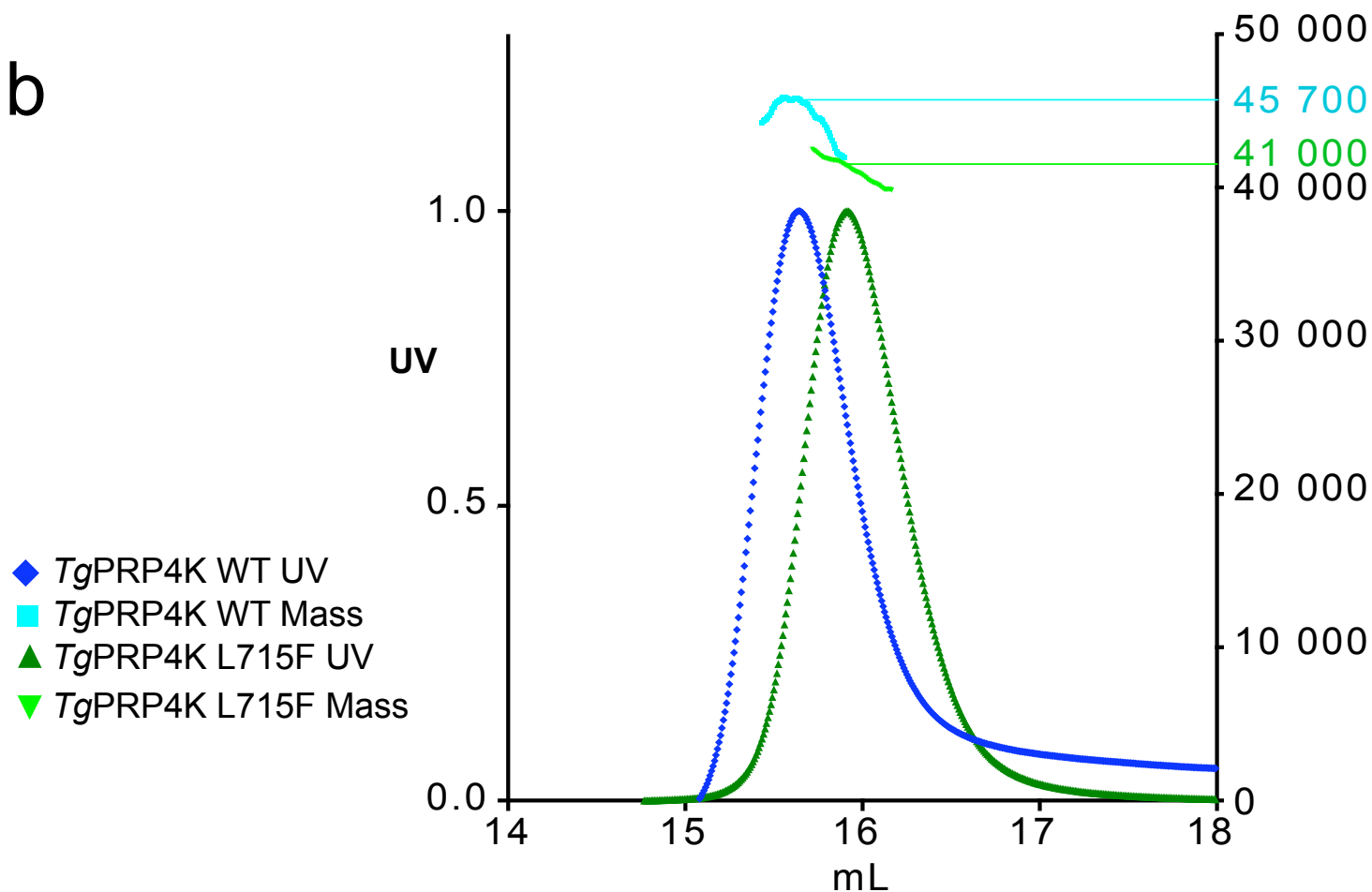


a**b****c**

a

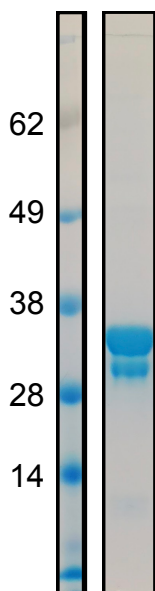


b

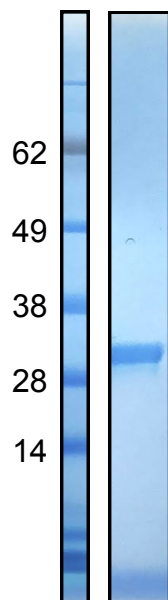


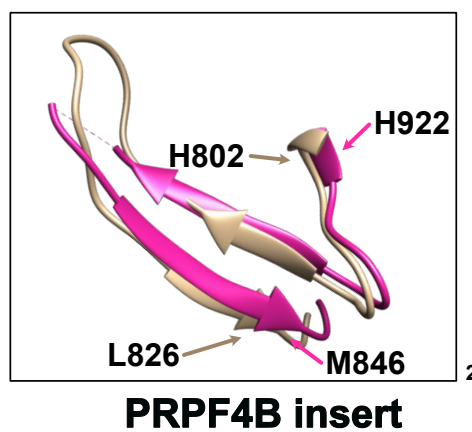
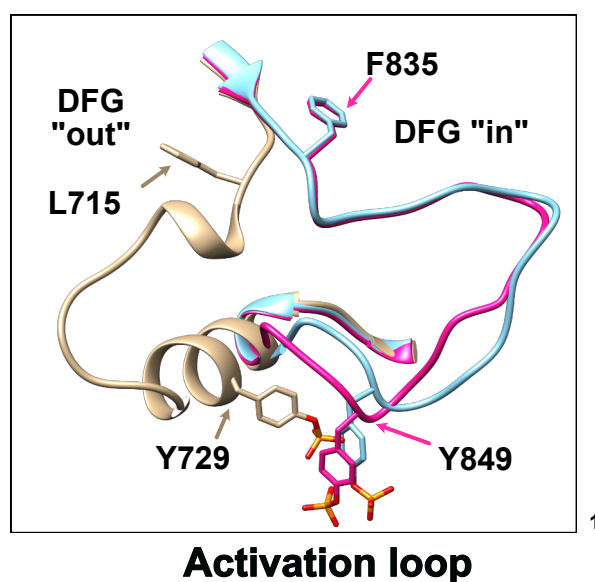
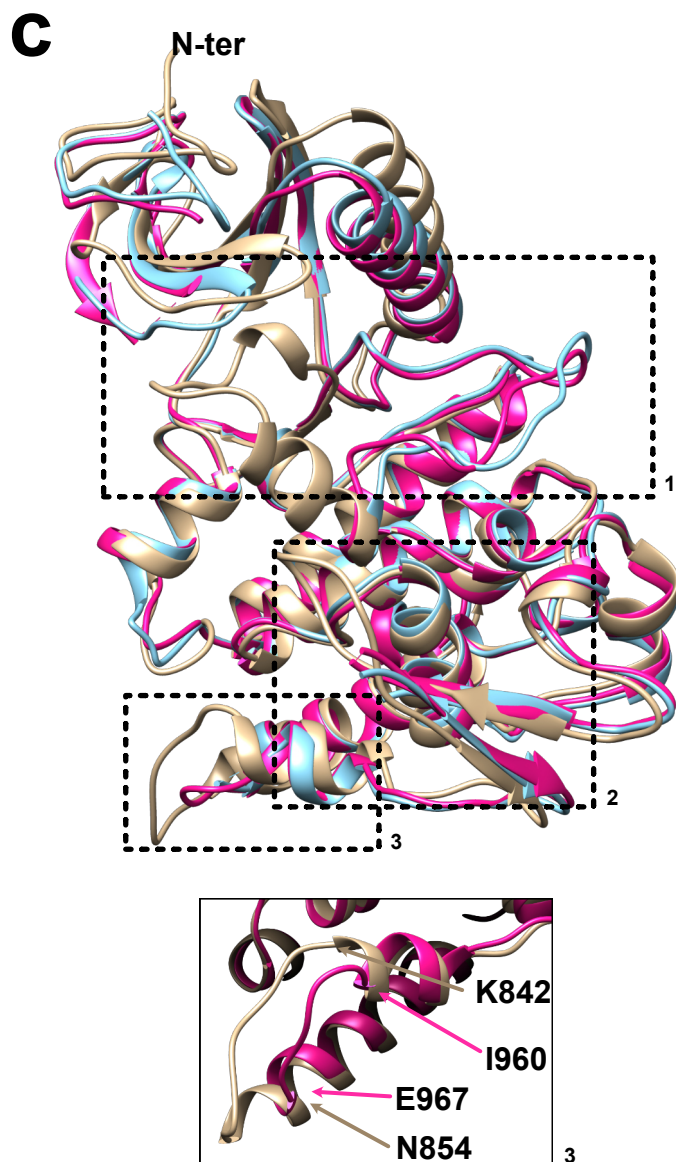
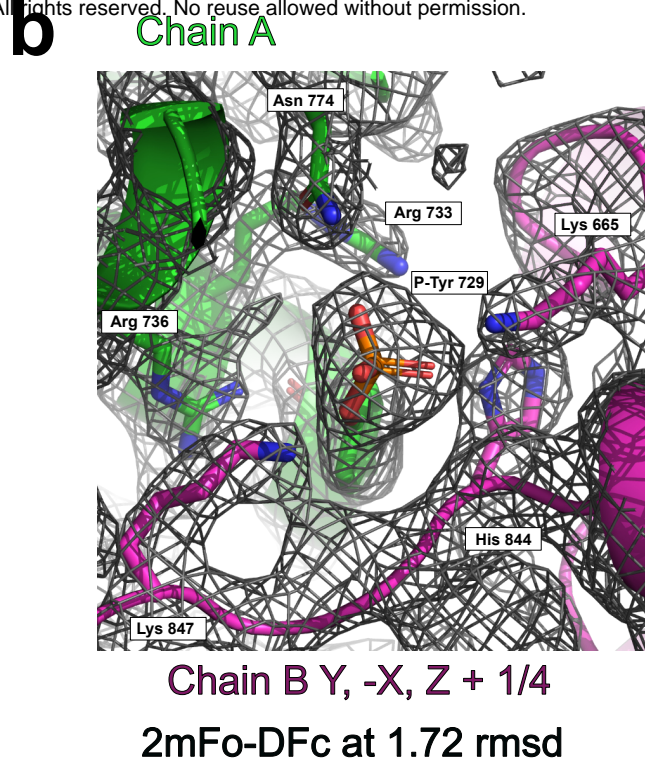
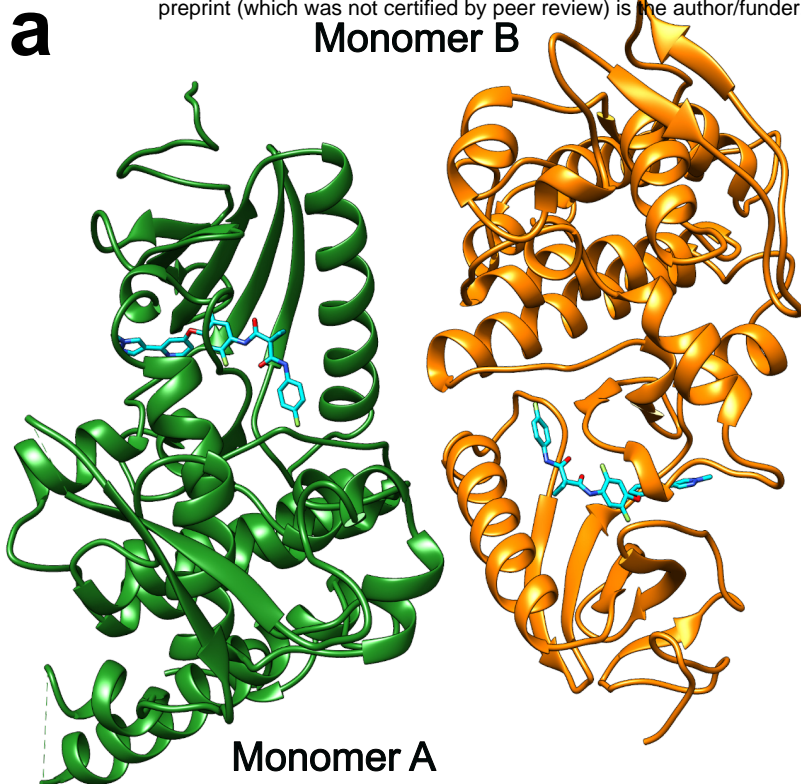
c

TgPRP4K
(aa 534-895)



TgPRP4K L715F
(aa 534-895)

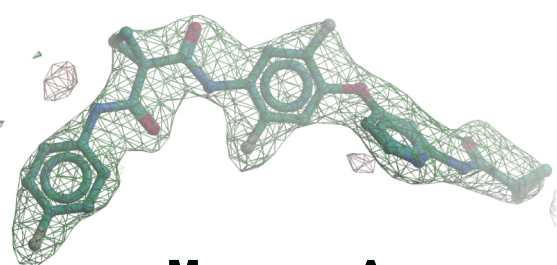




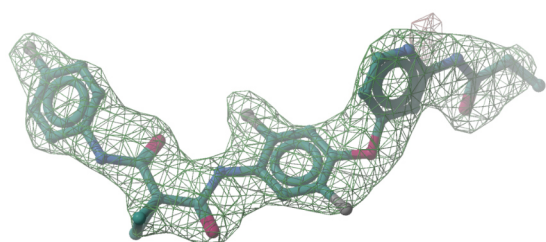
Toxo PRPF4B / altiratinib (this work)
Human PRPF4B / ADP (pdb id 4IFC)
Human PRPF4B / cmp 224 (pdb id 6PJJ)

a

mFo-DFc at 4.23 rmsd

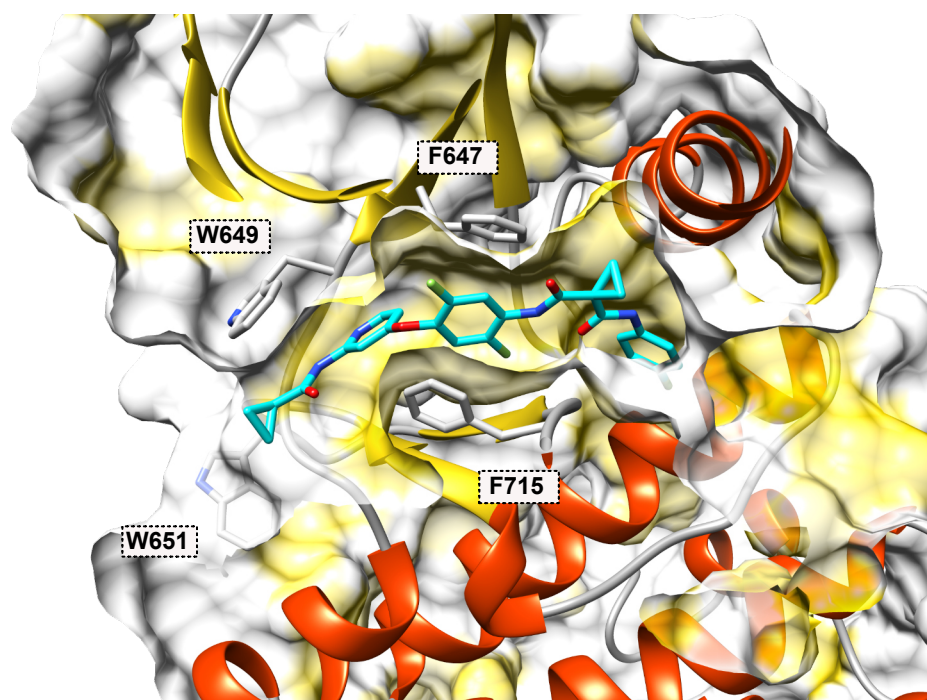


Monomer A

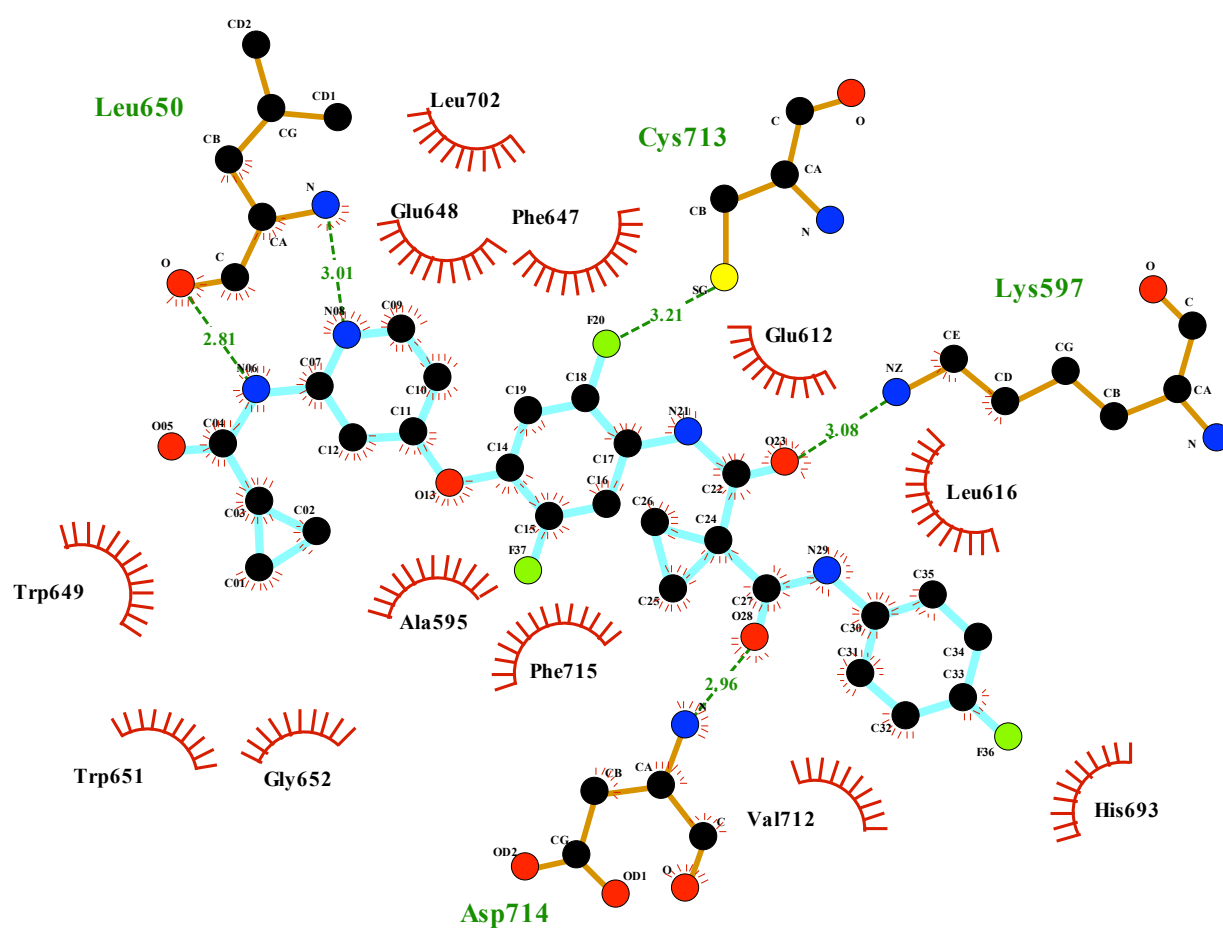


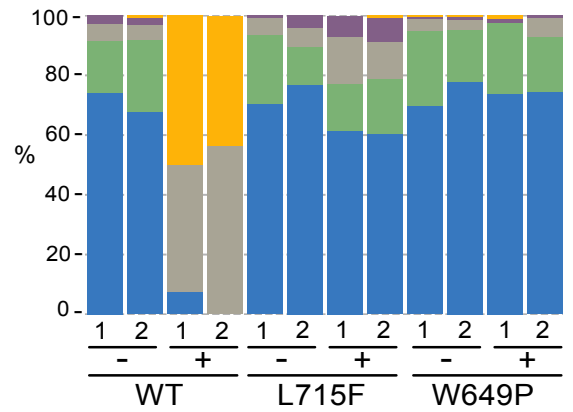
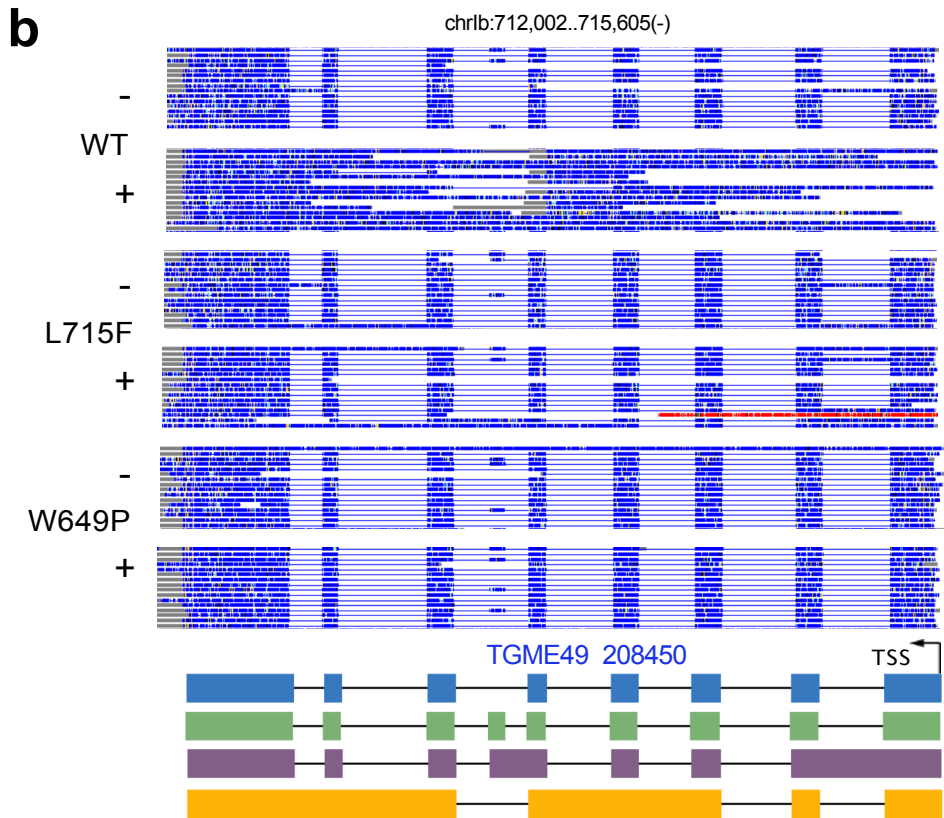
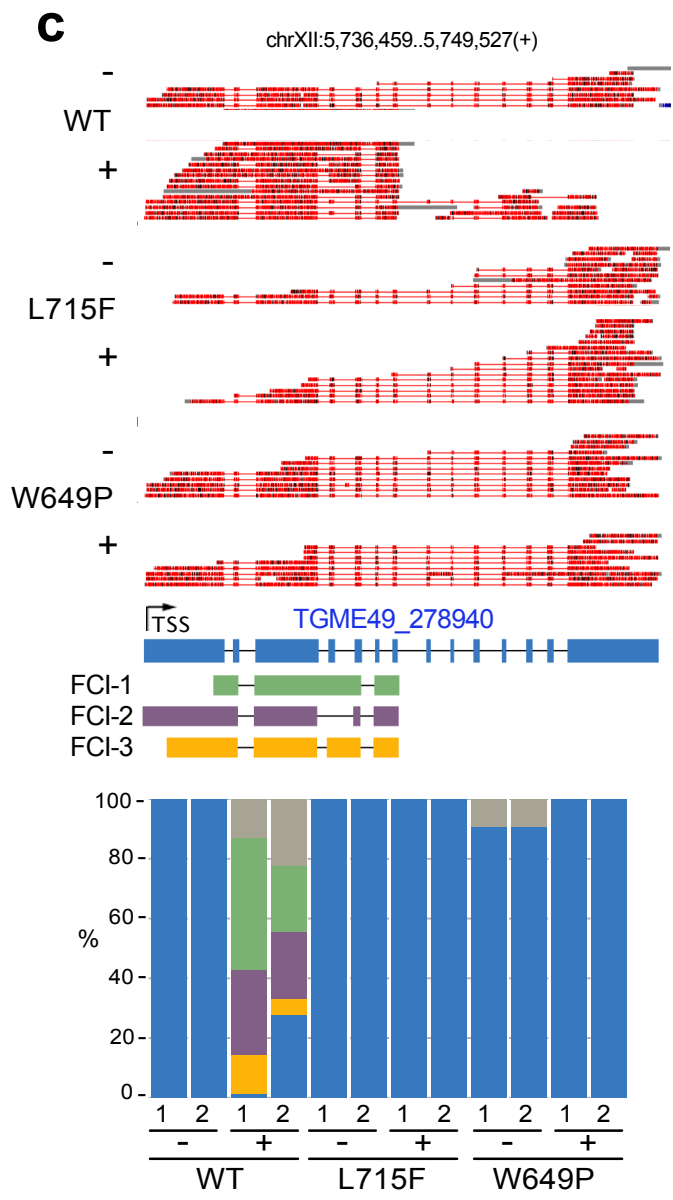
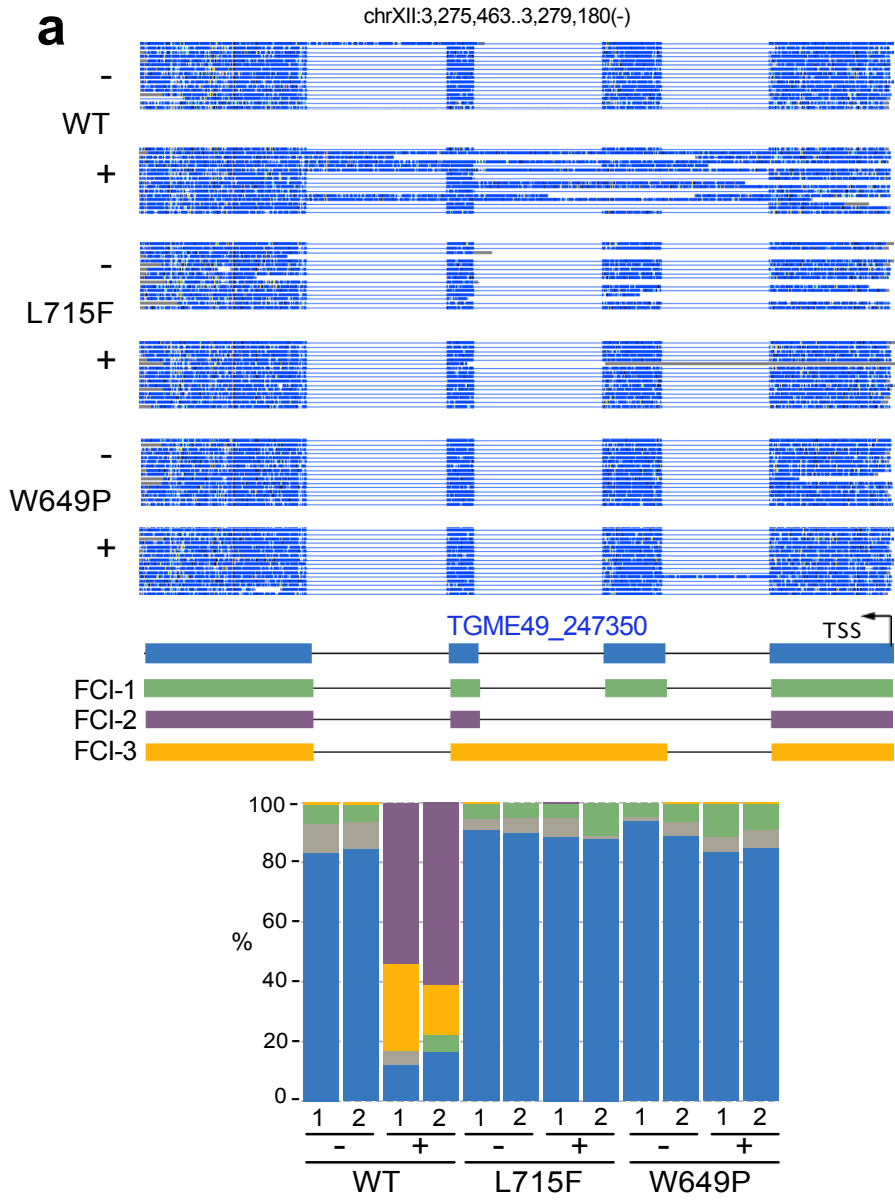
Monomer B

b

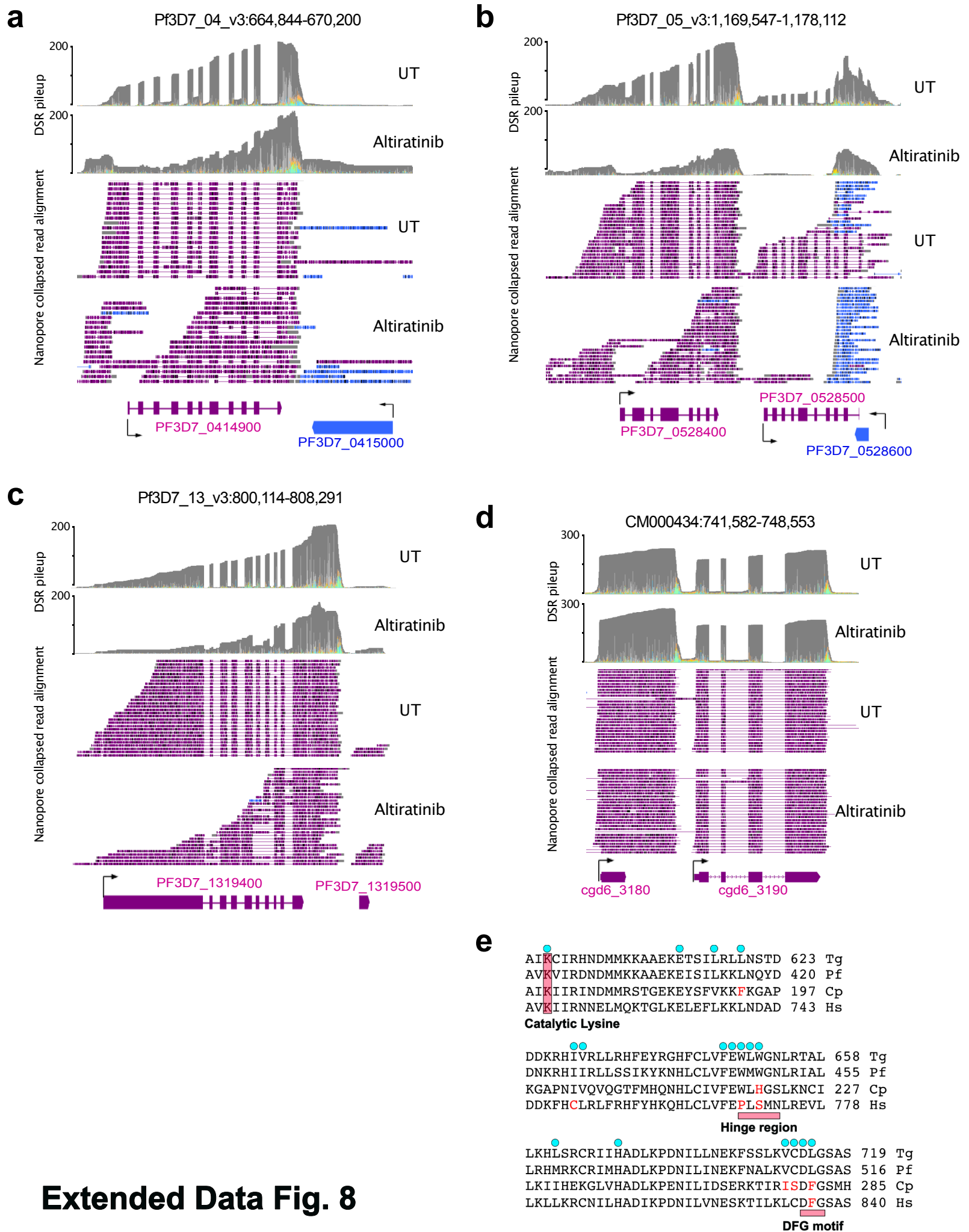


c

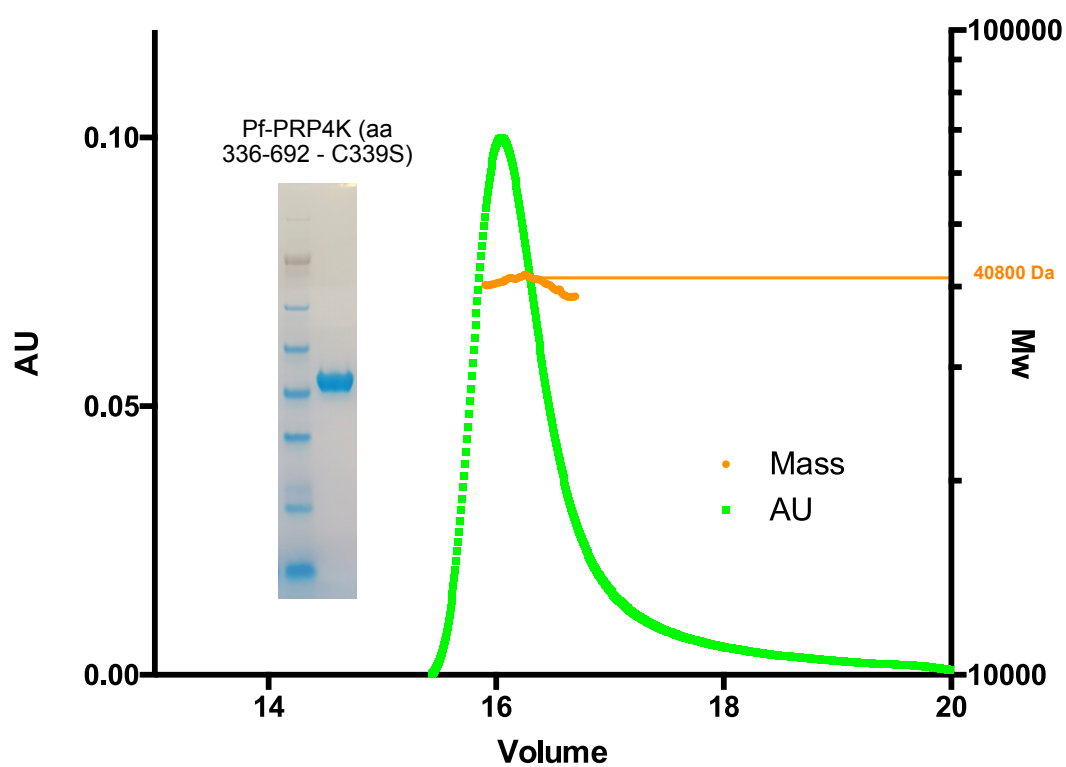




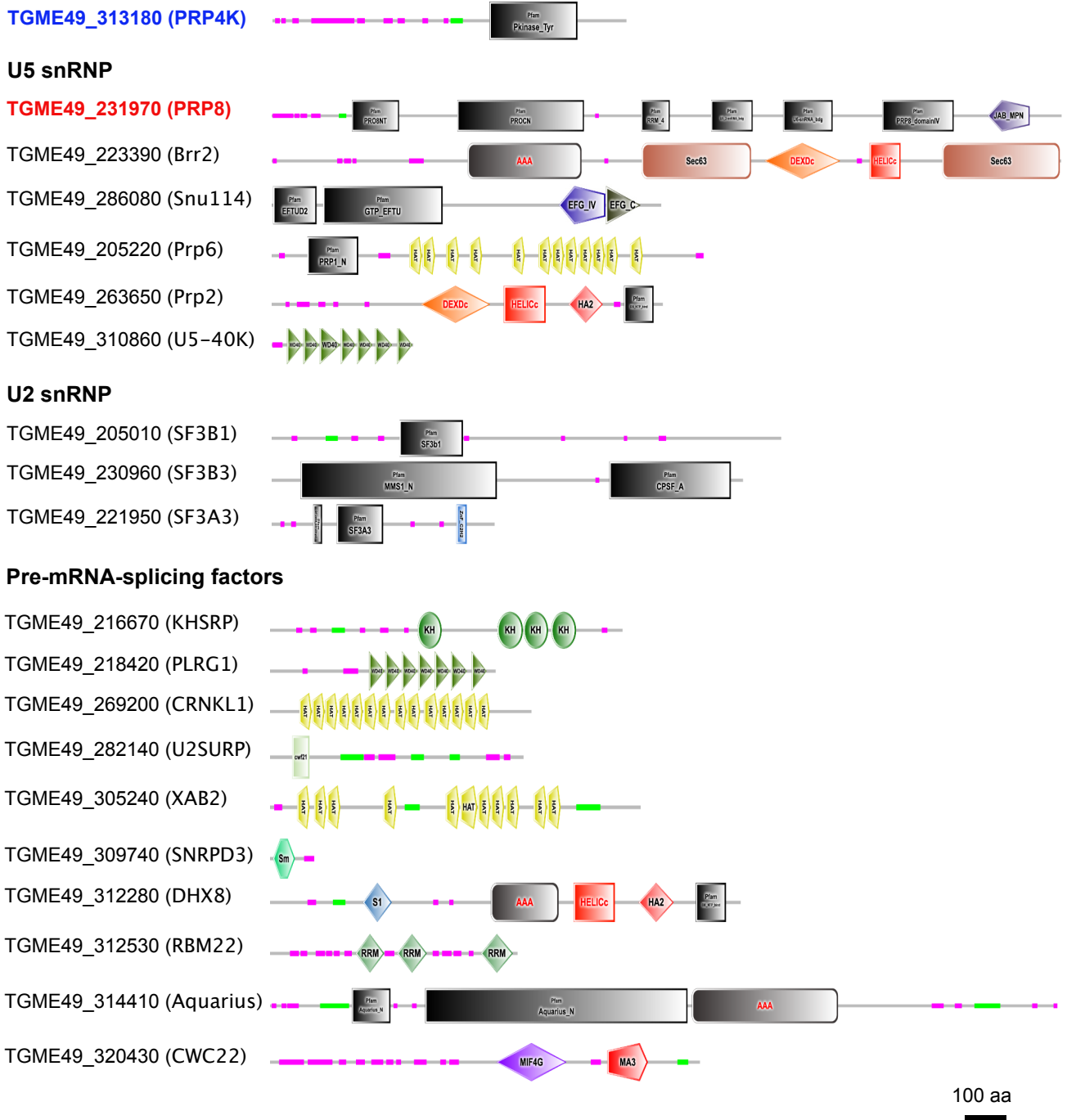
Extended Data Fig. 7



Extended Data Fig. 8



Extended Data Fig. 9



Supplementary Fig. 1